

1 **Impact of the Indian Ocean temperature - phytoplankton** 2 **feedback on simulated South Asia climate**

3
4 **Dmitry V. Sein^{1,2}, Anton Y. Dvornikov¹, Stanislav D. Martyanov¹, William Cabos³, Vladimir**
5 **A. Ryabchenko¹, Matthias Gröger⁴, Pankaj Kumar⁵**

6
7 ¹ Shirshov Institute of Oceanology, Russian Academy of Sciences; Moscow, Russia

8 ² Alfred Wegener Institute, Helmholtz Centre for Polar and Marine Research; Bremerhaven,
9 Germany

10 ³ University of Alcalá; Alcalá, Spain

11 ⁴ Leibniz Institute for Baltic Sea Research Warnemünde; Rostock 18119 Germany

12 ⁵ Indian Institute of Science Education and Research Bhopal; Bhopal, India
13

14 Corresponding author: Dmitry Sein (dmitry.sein@awi.de)

15 **Key Points:**

- 16 • Marine biogeochemical feedback leads to the decline of the SST during the phytoplankton
17 bloom and significant cooling of subsurface layers occurs
- 18 • The feedback leads to a drying over most of the area during the monsoon season
- 19 • The feedback's impact has cascading effects upon the model ocean physics which further
20 translates into altered atmosphere dynamics

21 **Abstract**

22 A regional Earth System Model has been implemented for the South Asia region. We investigate the
23 effect of the marine biogeochemical feedback which affects the attenuation of the short-wave
24 radiation upon the regional climate. In the experiment where the feedback is activated the average
25 SST is lower over most of the domain. The greatest deviations (more than 1°C) in SST between the
26 two runs observed in the summer period during the phytoplankton bloom. A significant cooling of
27 subsurface layers occurs and the thermocline shifts upward compared to the Jerlov type absorption.
28 The phytoplankton primary production and its deviation in the feedback-based simulation turned out
29 to be higher, especially during periods of winter and summer phytoplankton blooms. The marine
30 biogeochemistry feedback also affects the amount of precipitation in the model in particular during
31 the monsoon season. The associated SST cooling leads to a reduction of the precipitation but affects
32 it in different ways. In the Arabian Sea, the reduction of the transport of humidity across the equator
33 leads to a reduction of the large scale precipitation in the eastern part of the basin, reinforcing
34 reduction of the convective precipitation. In the Bay of Bengal, the feedback increases the large scale
35 precipitation, contouring the decrease of convective precipitation. Thus, the main impacts of
36 including the biogeochemical coupling in the Indian Ocean include the enhanced phytoplankton
37 primary production, a shallower thermocline and decreased SST, with cascading effects upon the
38 model ocean physics which further translates into altered atmosphere dynamics.
39

40 **Plain Language Summary**

41
42 The effect of the marine biogeochemical feedback on the South Asian regional climate has been
43 investigated. In the experiment where the feedback is activated the average surface temperature is
44 lower over most of the ocean. The greatest deviation is in the summer period during the phytoplankton

45 bloom. A cooling of subsurface layers occurs and the thermocline shifts upward compared to the
46 Jerlov type absorption. The phytoplankton primary production and its deviation in the feedback-based
47 simulation turned out to be higher, especially during periods of winter and summer phytoplankton
48 blooms. The marine biogeochemistry feedback also affects the amount of precipitation in
49 particular during the monsoon season. In the Arabian Sea, the reduction of the transport of humidity
50 across the equator leads to a reduction of the large scale precipitation in the eastern part of the basin,
51 reinforcing reduction of the convective precipitation. In the Bay of Bengal, the feedback increases
52 the large scale precipitation, contouring the decrease of convective precipitation. Thus, the main
53 impacts of including the biogeochemical coupling in the Indian Ocean include the enhanced
54 phytoplankton primary production, a shallower thermocline and decreased sea surface temperature.
55

56 **1. Introduction**

57 The vulnerability and the ability of society and natural systems to adapt to the impact of
58 climate change vary greatly according to geographic regions and populations. The Indian
59 subcontinent and adjacent area, where a fifth of humanity lives, is one of the regions where the
60 impacts are strong both in the present time and future climate projections (Turco et al, 2015; Szabo
61 et al., 2016). The strongest impacts are related to changes in the intensity and frequency of extreme
62 events (such as floods, droughts, tropical cyclones, storm surges, phytoplankton blooms, ocean heat
63 waves, avalanches, etc.) which can inflict significant damage on ecosystems, human populations,
64 infrastructure and property. In particular, the intensity of extreme events over India is increasing
65 continuously, a fact which can be observed every year when one or other region gets affected by
66 floods causing enormous socio-economic losses (IPCC AR5, 2014).

67 Atmospheric extreme events contribute to the emergence of extreme situations in the ocean
68 and vice versa. For example, the strengthening of the southwestern monsoon in the Arabian Sea leads
69 to abnormal coastal upwelling and increased mixing of the upper ocean layer, the subsequent supply
70 of nutrients into the upper layer from the deep ocean and anomalous blooms of phytoplankton
71 (Ryabchenko et al., 1998). In turn, the changes in sea surface temperature (SST) and surface fluxes
72 of heat and momentum caused by monsoons can feedback to atmospheric circulation. It is known that
73 the Bay of Bengal is one of the main tropical cyclogenesis areas in the world (Dube et al., 1997).
74 Strong cyclones forming here lead to catastrophic storm surges during which hundreds of thousands
75 of people lose their lives (Tasnim et al., 2015). Another example of the relationship between
76 atmospheric and oceanic processes is associated with river runoff and nutrient loading which is
77 projected to be maximum in southern and eastern Asia due to the growth of population and increased
78 industrialization (Seitzinger et al., 2002). The Ganges–Brahmaputra estuary is strongly vulnerable to
79 high nutrient load from river discharges (Seitzinger et al., 2005; Mukhopadhyay et al., 2006). Global
80 warming can enhance the freshwater river runoff and the nutrient flux thus enhancing the primary
81 production in coastal areas. It was stated that the estuarine ecosystem experiences a complete change
82 in terms of phytoplankton during monsoon (De et al., 2011) and that the eastern Indian coast is
83 affected by localized eutrophication which directly influences the nutrient level of coastal water and
84 phytoplankton abundance (Choudhury & Pal, 2010). Recent assessments (Sattar et al., 2014) of the
85 impact of food production upon the river flux of nutrients into the Bay of Bengal coastal waters in
86 the past and the future show that the coastal eutrophication potential is high in the Bay of Bengal thus
87 elevating the risk for oxygen deficiencies (d'Asaro et al., 2019). The above examples of interactions
88 between atmospheric and oceanic processes underscore the need to create a unified high-resolution
89 modeling system for the region to be able to study these interactions in detail.

90 Earth System Models (ESMs) include coupled representations of the ocean, atmosphere, land
91 use, vegetation, biogeochemistry, atmospheric chemistry, and the hydrological cycle. They are very

92 effective tools for the study of the Earth's climate system and are used to investigate the complex
93 systems and associated mechanisms in climate and environmental sciences in the past and future,
94 driven by assumptions on the evolution of climate change (Taylor et al., 2012). However, they usually
95 lack the resolutions that are necessary for regional studies. Dynamical downscaling with Regional
96 Climate Models (RCMs) is used to translate the global climate information generated by ESMs down
97 to regional scales at a higher resolution. RCMs take the initial conditions and time-dependent
98 boundary conditions from the global models and provide dynamically downscaled climate
99 information within the region of interest (Giorgi, 2006).

100 We have implemented a new version of the high-resolution Regional Earth System Model
101 (RESM) ROM (Sein et al., 2015) for South Asia and the northern Indian Ocean. The model includes
102 ocean, atmosphere, hydrological cycle and marine biogeochemistry components. Such a modeling
103 system is required for the study of extreme events in the atmosphere and the ocean in the India region
104 for seasonal and decadal predictions, climate change projections and advanced monsoons modeling.
105 It will help to better describe their interaction with the ocean and glaciers, calculate their statistical
106 characteristics and fulfill projections for the future.

107 In this study we will use the model to assess the impact of marine biogeochemical feedback
108 upon the simulation of the present climate over the Indian subcontinent and the adjacent ocean using
109 the South Asia CORDEX domain. To this end, we compare two simulations carried out with our
110 RESM. In both simulations, the model is driven by data from CMIP5 20th century simulation with
111 the Max Planck Institute Earth System Model (MPI-ESM). These two simulations differ only in the
112 influence of the ocean biochemistry module on the shortwave solar radiation penetration into the
113 ocean. In the first simulation, we use a light attenuation parameterization based on the Jerlov water
114 types, when the attenuation coefficient depends on the water type specified but does not vary in time.
115 The use of Jerlov water types is the standard case in ocean modelling although it has several
116 shortcomings. Firstly, the dynamics of phytoplankton blooms on the light climate is completely
117 neglected, which is highly problematic in regions which are subject to a strong seasonal cycle and in
118 regions with strongly varying nutrient supply. Secondly, coastal characteristics, especially in front of
119 large rivers with high nutrient load and limited exchange with the open ocean, are not resolved which
120 is however important in high resolution downscaling simulations. In the second simulation, we
121 introduce the marine biogeochemical feedback by calculating the attenuation coefficient using the
122 phytoplankton concentration simulated by the ocean biogeochemistry module and allow to feedback
123 onto the absorption of shortwave radiation by the physical module (MPIOM). Hence, the presence of
124 a strong local phytoplankton bloom in the surface layer will increase the heat absorption in the upper
125 layers and decrease it in deeper layers, with cascading feedbacks on the thermohaline structure of the
126 water column such as the e.g. thermocline intensity and depth. Due to these reasons in regional
127 climate studies, the effect of seasonal and local varying phytoplankton concentration can be expected
128 to be important. The reason why so many ocean models make use of the more simple Jerlov
129 attenuation scheme is not a scientific one but is of economic nature. Including the biogeochemical
130 feedback, as done here, requires online coupling to a biogeochemistry model which leads to a
131 threefold consumption of CPU hours compared to an uncoupled model running with Jerlov water
132 types.

133 The objectives of this paper can be summed as follows:

- 134 1. To evaluate the ability of our model to reproduce the present climate in the South Asia
135 CORDEX region both in the ocean and the atmosphere.
- 136 2. To evaluate the quality of corresponding simulated physical and biogeochemical
137 characteristics in the northern part of the Indian Ocean.

- 138 3. To assess the impact of the biochemistry feedback upon the simulated regional climate,
139 both in the atmosphere and the ocean.

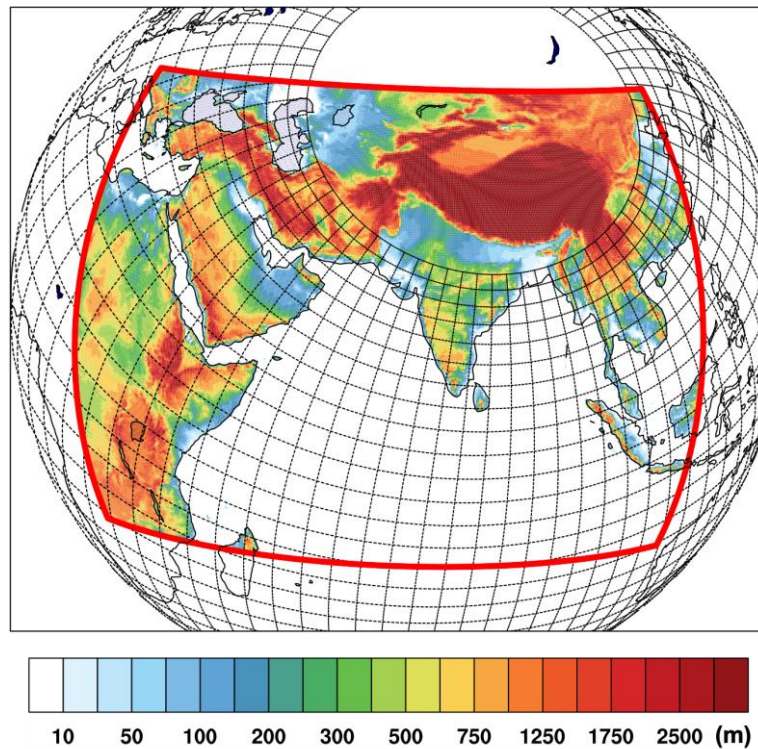
140 The layout of the present paper is as follows. In section 2 a description of the coupled modeling
141 system is presented. Section 3 is focused on the verification of the developed RESM and its results.
142 Section 4 contains some discussion. Conclusions are presented in section 5.

144 2. Methods

145 The oceanic component of our RESM ROM is the Max Planck Institute Ocean Model
146 (MPIOM: Marsland et al., 2002; Jungclaus et al., 2013). Via the OASIS coupler, the MPIOM is
147 coupled with the REgional atmospheric MOdel (REMO: Jacob, 2001), the Hamburg Ocean Carbon
148 Cycle model (HAMOCC: Ilyina et al., 2013), and the Hydrological Discharge model (HD: Hagemann
149 and Dumenil, 1998). This coupled modeling system has the distinctive feature that its global ocean
150 module provides the possibility to refine the grid resolution in the region of interest and to avoid the
151 lateral boundary conditions in the ocean while performing calculations. Another feature of the ROM
152 is that the dynamical link between the ocean and the atmosphere (coupling) is implemented only at
153 the chosen subdomain, while outside this region in the uncoupled area the ocean module of the ROM
154 system calculates heat, freshwater, and momentum fluxes from atmospheric fields taken from the
155 same global model used for REMO boundary conditions. A detailed description of the coupled model
156 ROM can be found in (Sein et al., 2015).

157 For this study, we perform two present-time simulations using ROM. The setups used are
158 almost identical and differ only in the activation of the ocean biogeochemistry component. For REMO
159 we use the slightly extended CORDEX (<http://www.cordex.org>) South Asia domain (Fig. 1). The
160 mesh of the global oceanic component has a variable horizontal resolution which reaches up to 15
161 km inside the coupled region. In both simulations, the model is driven by data from a historical
162 simulation with the MPI-ESM LR setup. The model runs were performed for the period 1920–2005,
163 the first 30 years being an adjustment period. Initial conditions for the biogeochemical module were
164 taken from MPIOM/HAMOCC long term simulations (Gröger et al., 2013). For the ocean and
165 atmosphere, the initial conditions were taken from previous spin-up simulations: 50 years MPIOM
166 stand-alone run plus 2 times 40 years (80 years) coupled MPIOM/REMO simulations with ERA-
167 Interim forcing.

168



169
 170 **Figure 1.** ROM configuration. The red frame shows the coupled ocean-atmosphere CORDEX domain. The
 171 black lines indicate the grid of the MPIOM/HAMOCC models (only every 12th line is shown). Color scale
 172 represents orography.

173
 174 The two ROM simulations (labeled as INDJ and INDB hereafter) differ by various
 175 parameterizations of the attenuation of short-wave radiation (SWR) penetrating into the ocean and its
 176 influence on water temperature. In the INDJ experiment, the model utilized a simple classical light
 177 attenuation parameterization based on the Jerlov water types (Jerlov, 1976). In this case, the
 178 attenuation coefficient depends on the water type specified in the model, but does not vary in time.
 179 This light attenuation parameterization was used both for the evolutionary equation for water
 180 temperature and in the HAMOCC marine biogeochemical module which is forced by the ocean but
 181 does not have the feedback to the ocean. In the INDB experiment, the biogeochemical feedback
 182 between the ocean and the atmosphere through the marine ecosystem was implemented by making
 183 the light attenuation coefficient a function not only of water attenuation itself but also phytoplankton
 184 concentration (Gröger et al., 2013). In the INDB run, this parameterization was implemented in both
 185 the physical and biogeochemical blocks of the ocean model. Therefore, in the INDB experiment, the
 186 presence of phytoplankton in the water reduces the amount of SWR penetrating into the deeper layers
 187 thus affecting the water column temperature and, through water temperature, the heat flux between
 188 the ocean and the atmosphere.

189
 190 **3. Results**

191 **3.1 Ocean**

192 To verify the model we use the temperature, salinity, dissolved nitrates and dissolved
 193 phosphates data from the World Ocean Atlas 2013 (WOA13), and chlorophyll concentration from
 194 the satellite data (SeaWiFS and MODIS-Aqua).

195 According to the India Meteorological Department, we distinguish the following seasonal
 196 periods used for the verification procedure based on the monsoon activity in the northern part of the
 197 Indian Ocean:

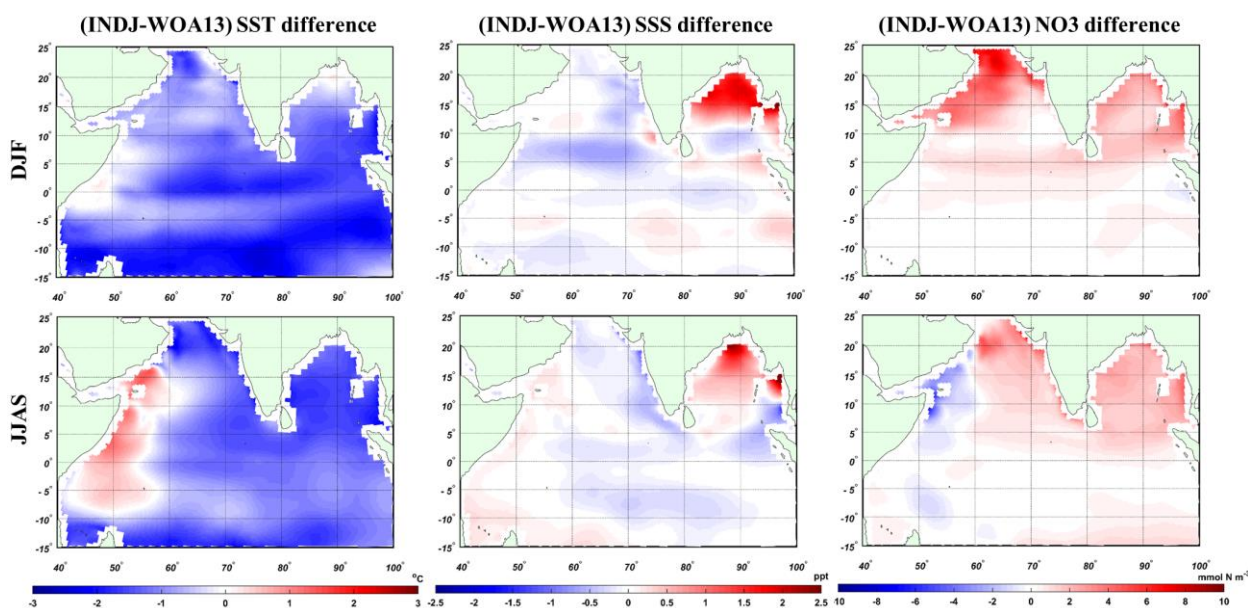
- 198 • DJF: December–February (winter season, NE winds);
- 199 • MAM: March–May (pre-monsoon season);
- 200 • JJAS: June–September (monsoon season, SW winds);
- 201 • ON: October–November (post-monsoon season);

202 In the following, we compare the model results and observations for winter (DJF) and summer
 203 (JJAS) seasons time-averaged over 1975–2004, since the phytoplankton impact is expected to be
 204 maximal during the bloom periods.

206 3.1.1 Sea surface

207 *Sea surface temperature and salinity (SST and SSS).* Figure 2 shows the spatial distribution of
 208 the difference between the modeled SST, SSS and corresponding WOA13 data for the winter (DJF)
 209 and summer (JJAS) climatic seasons time-averaged over 1975–2004. It can be seen that the model
 210 generally underestimates the SST relative to the observational climatic data, the exception being the
 211 region located off the coast of the Somali peninsula. The largest deviations in SSS from the WOA13
 212 are observed in the Bay of Bengal, salinity being overestimated by the model by 0.5–2‰ in the
 213 surface layer. The largest discrepancy in SSS occurs in winter (DJF), while in pre-monsoon and
 214 monsoon seasons the maximum difference is about 0.5‰ and 1.5‰, respectively. Off the western
 215 Indian coast, calculations show somewhat lower SSS than that in the WOA13 surface salinity field,
 216 the largest discrepancy here between ROM and WOA13 occurring in autumn and being up to 1‰
 217 (not shown).

218



219

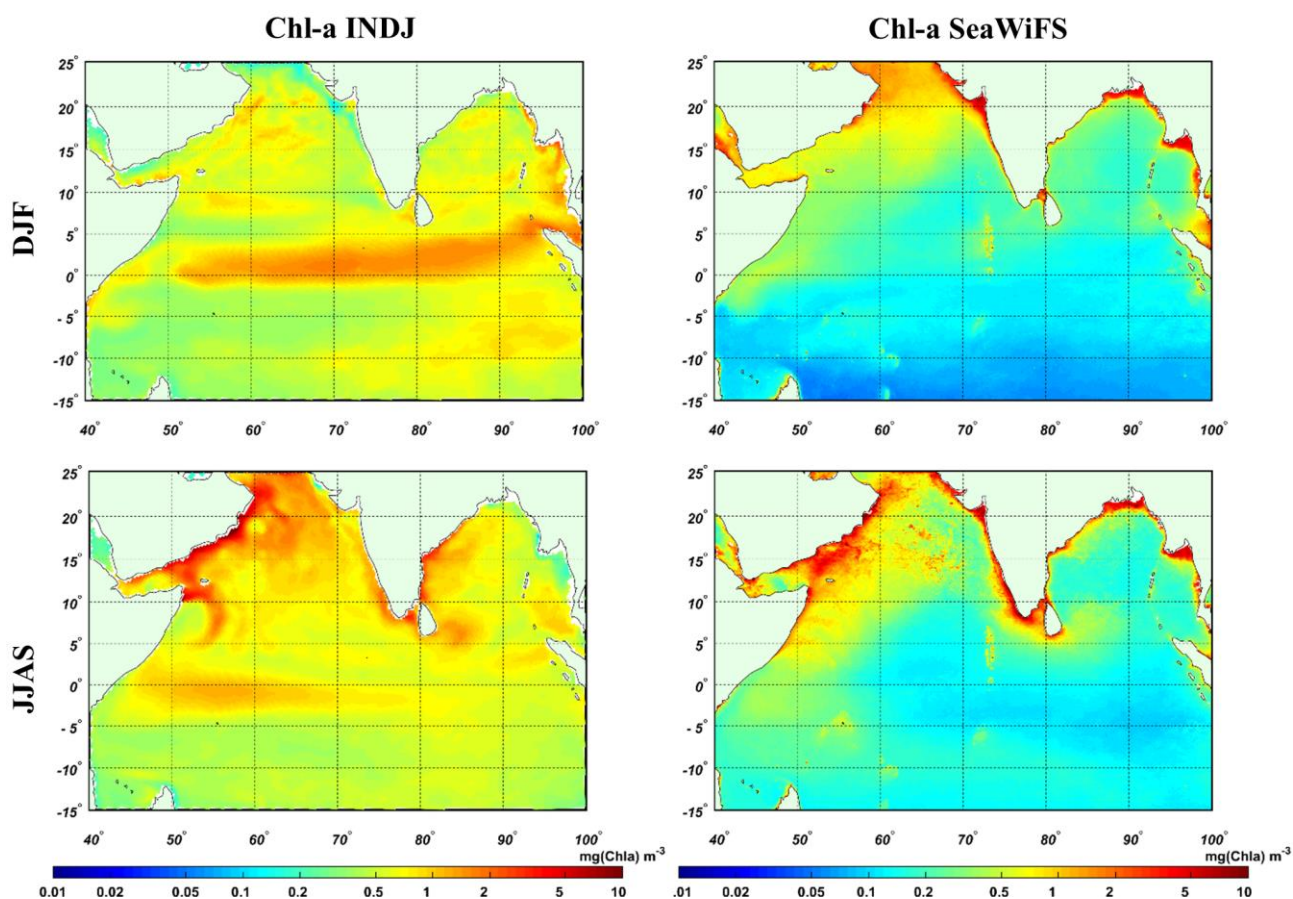
220 **Figure 2.** Spatial distribution of the difference between experiment INDJ and WOA13 for SST (left column),
 221 SSS (middle column) and NO3 in the surface layer (right column). SST, SSS and NO3 are time-averaged for
 222 winter (DJF) and summer (JJAS) for the period 1975–2004.

223

224 *Sea surface concentration of dissolved nitrate.* It was found that, compared to WOA13, the
 225 HAMOCC biogeochemical model somewhat overestimates the surface concentration of nitrates
 226 (NO3), especially during winter (Fig. 2). The strongest deviations are located along the coasts and
 227 are related to uncertainties in nutrient supply originating from rivers and point sources as we apply a
 228 rough climatological estimate for external nutrient supply (Gröger et al., 2013). With more distance
 229 from the coasts, the model bias reduces showing the model’s capability to correctly simulate the

230 biogeochemical cycling of the open Indian ocean which is the main purpose of this study. In front of
 231 NE Africa and South Arabia, the modeled too high SSTs and too low nitrate concentrations during
 232 the summer monsoon season may indicate too weak upwelling in response to the predominant SW
 233 wind regime. At a depth of 50 m, the agreement between WOA13 and the model is somewhat better
 234 and the main features of the spatial distribution of nitrates are reproduced correctly. The only serious
 235 exception is the overestimated concentration of nitrates in autumn off the southwest coast of India.
 236 At a depth of about 100 m, the discrepancy between the WOA13 data and the model is more
 237 pronounced. At a depth of 500 m the WOA13 and modeled nitrates are very similar, which is
 238 obviously due to the small influence of the seasonal ecosystem dynamics upon the distribution of
 239 nitrates at such depths. The maximum deviations in surface nitrate field between the model and
 240 WOA13 data occur during the bloom periods (winter and summer) in both simulations (INDJ and
 241 INDB), while this deviation is minimal in spring. In general, the modeled annual surface
 242 concentration of dissolved nitrate is slightly higher than in WOA13.

243 *Sea surface chlorophyll-a concentration.* Verification of the biogeochemical module
 244 HAMOCC was also made based on the ocean surface chlorophyll-a concentration (Fig. 3). The
 245 calculated surface phytoplankton concentration (in carbon units) was converted into the chlorophyll-
 246 a concentration (in mg/m^3) using the constant C:Chl ratio equal to 60 gC / gChl used in HAMOCC
 247 (Ilyina et al., 2013).
 248



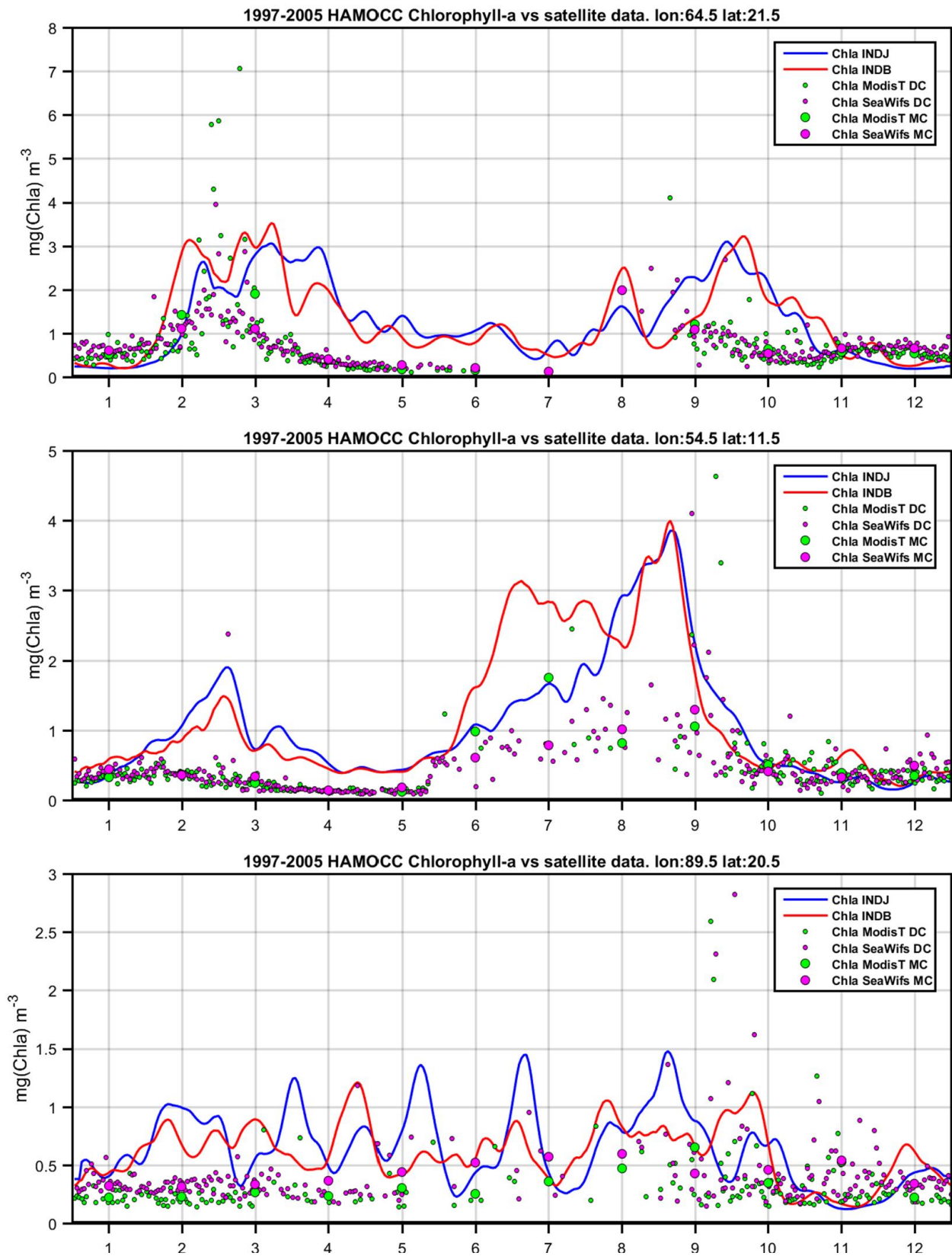
249 **Figure 3.** Comparison of the simulated (INDJ) and observed (SeaWiFS) surface chlorophyll-a concentration.
 250 The fields are time-averaged seasonally (DJF, JJAS) for the period 1997–2005.
 251
 252

253 It is clear that the modeled chlorophyll-a concentration is overestimated in comparison with
 254 the SeaWiFS satellite data. Still, according to SeaWiFS, the model captures the main patterns in the
 255 spatial distribution of chlorophyll-a concentration in the surface layer during the periods of maximum

256 phytoplankton development (bloom in JJAS, Fig. 3). To the north of 5°N, both the model and the
257 satellite data show the seasonal dynamics of chlorophyll-a. The model produces lower chlorophyll-a
258 concentrations in the Arabian Sea under the predominant NE wind regime during the winter monsoon,
259 compared to SeaWiFS data. By contrast, SW winds during the summer monsoon induce upwelling
260 of nutrients from deeper layers and stimulate primary production. In the model, the enhanced
261 chlorophyll-a concentrations occur during winter along the eastern boundary of the Bay of Bengal
262 while reduced production is indicated there during summer. While these changes are in accordance
263 with the changing wind regime, the satellite data show higher concentrations also during summer.
264 The most plausible explanation for this is a persistently high supply of riverine nutrients around the
265 year. Another difference between the model and satellite data is the presence of increased chlorophyll-
266 a concentration zone stretching along the equator in the model results, especially during the winter
267 period. It is not present in satellite data. We think that the cause is the overestimated upwelling in the
268 equatorial region and, thus, the enhanced supply of nutrients to the surface. The overestimation or
269 underestimation of ocean productivity along the equatorial divergence zone is a common problem of
270 many ocean general circulation models (e.g., Steinacher et al., 2010).

271 A comparison of the time-series of the HAMOCC surface chlorophyll-a concentration with
272 satellite data was also carried out (Fig. 4).

273



274
 275 **Figure 4.** Comparison of the simulated (INDJ and INDB) and observed (SeaWiFS, MODIS Terra) time-series
 276 of surface chlorophyll-a concentration in the Arabian Sea (a), Somali upwelling area (b), and the Bay of Bengal
 277 (c).

278
 279 **3.1.2 Vertical distributions**

280 *Vertical distribution of water temperature, salinity and nutrients.* We have also analyzed the
 281 spatially-averaged vertical profiles of water temperature, salinity and dissolved nitrate and

282 phosphorus concentration for the northern part of the Indian Ocean (IO) and for the Arabian Sea
283 (ASF) and the Bay of Bengal (BBF) regions (Fig. 5).

284

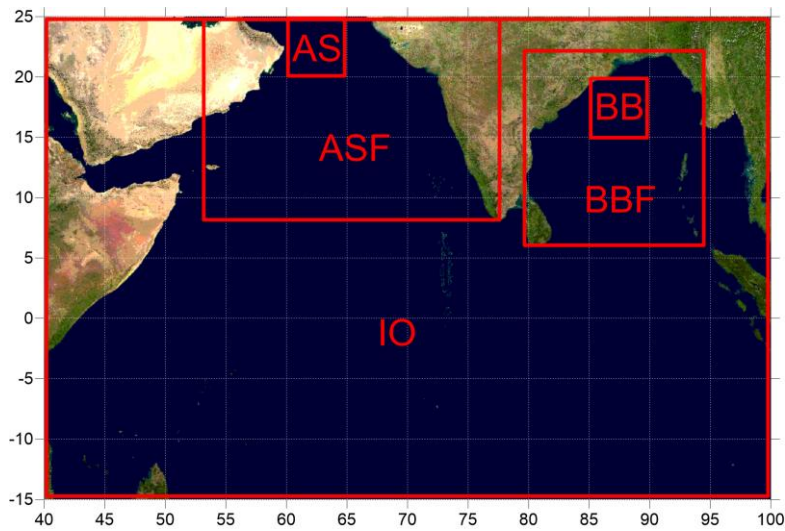


Figure 5. Spatially-averaged areas in the model domain.

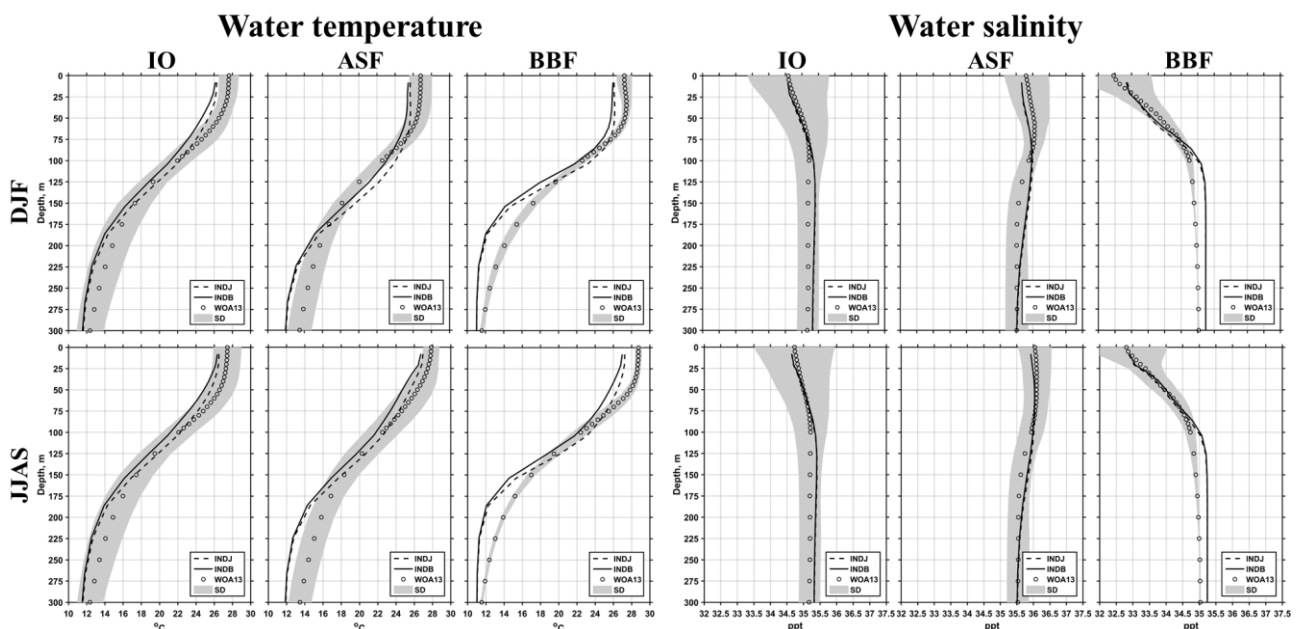
285

286

287

288 As seen from Fig. 6, the simulated vertical distribution of temperature and salinity is in
289 relatively good agreement with WOA13 data. The modeled values are generally within the standard
290 deviation range of the corresponding WOA13 data. The results are close to the climatic in the Arabian
291 Sea and in the Bay of Bengal but they are out of the standard deviation range there in most cases.
292 Still, it should be noted that the standard deviation of WOA13 data is very small in these areas due to
293 the scarcity of observations. The same is true for the vertical distribution of nutrients (Fig. 7).

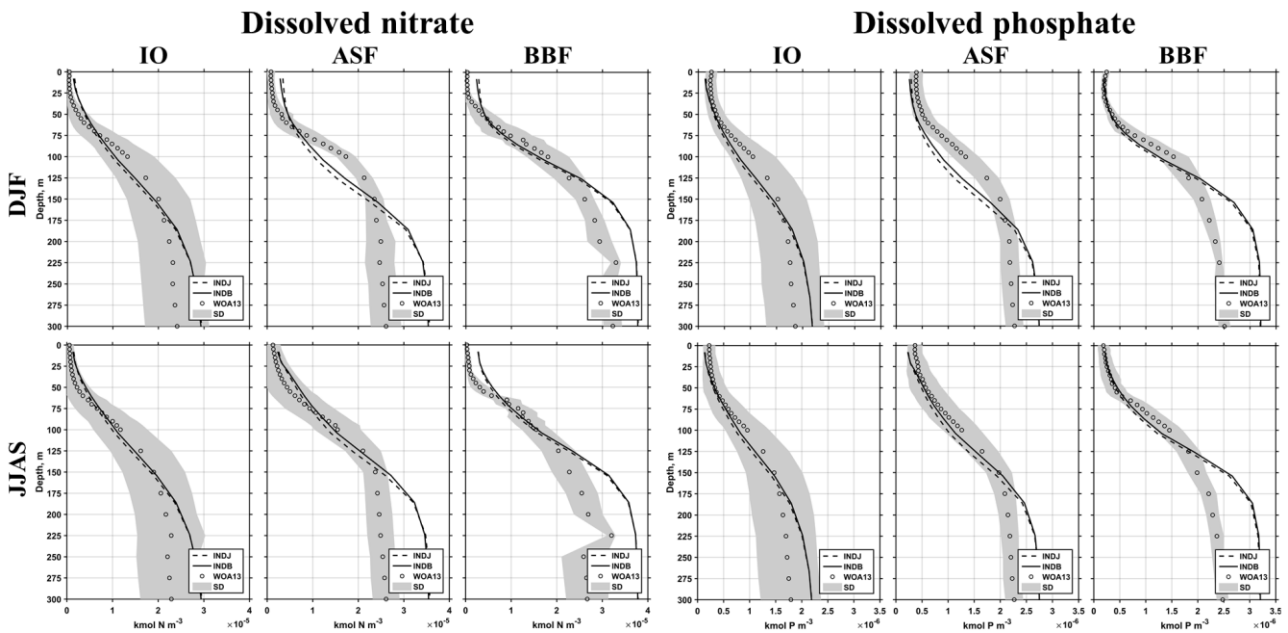
294



295 **Figure 6.** Vertical profiles of water temperature and salinity time-averaged seasonally (DJF, JJAS) for the
296 period 1975–2004. INDJ and INDB designate the model runs; WOA13 designates the climatic data from the
297 World Ocean Atlas 2013; SD designates the standard deviation of the WOA13 data.

298

299



300
 301 **Figure 7.** Vertical profiles of dissolved nitrate and phosphate time-averaged seasonally (DJF, JJAS) for the
 302 period 1975–2004. INDJ and INDB designate the model runs; WOA13 designates the climatic data from the
 303 World Ocean Atlas 2013; SD designates the standard deviation of the WOA13 data.

304

305

3.1.3 Impact of the marine biogeochemistry feedback

306

307

308

309

310

311

312

313

314

315

316

317

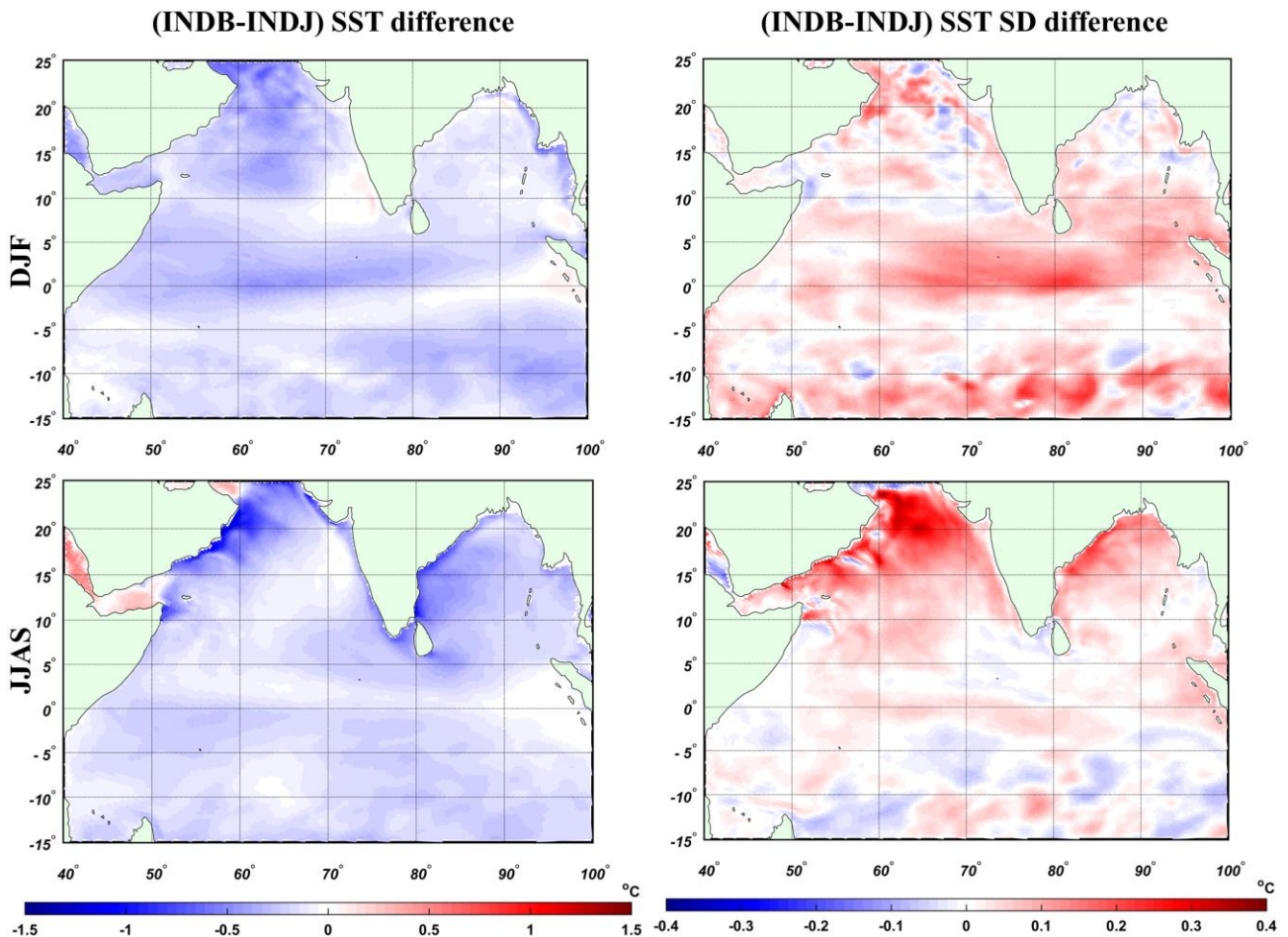
318

319

320

321

Impact of the feedback on the water temperature and salinity. We have also compared the results of two model runs (INDJ and INDB) between each other in order to investigate the impact of the chlorophyll-dependent light attenuation parameterization (Gröger et al., 2013) upon the main oceanic variables. The vertical distribution of temperature, salinity, dissolved nitrate and phosphate for different regions of the model domain was already presented in Fig. 6–7 for both experiments. Figure 8 shows the spatial distribution of the climatological (1975–2004) values of the SST difference between the two model runs (INDB-INDJ), as well as the difference in SST standard deviation for both experiments. In winter (DJF) the feedback between the ocean and the atmosphere through the marine ecosystem leads to the colder SST, with differences reaching up to 1° C in the northern part of the Arabian Sea. The exceptions are the areas near the southwestern coast of India, the northwestern coast of Indonesia and the eastern part of the Andaman Sea. But the SST increase in these areas is insignificant and does not exceed 0.1° C. In summer (JJAS) the difference in SST between the two runs is even more pronounced, especially in the northern part of the Arabian Sea and along the eastern coast of India. SST in the INDB experiment is also characterized by stronger variability, the standard deviation of temperature fluctuations being higher by approximately 0.3° C compared to INDJ.

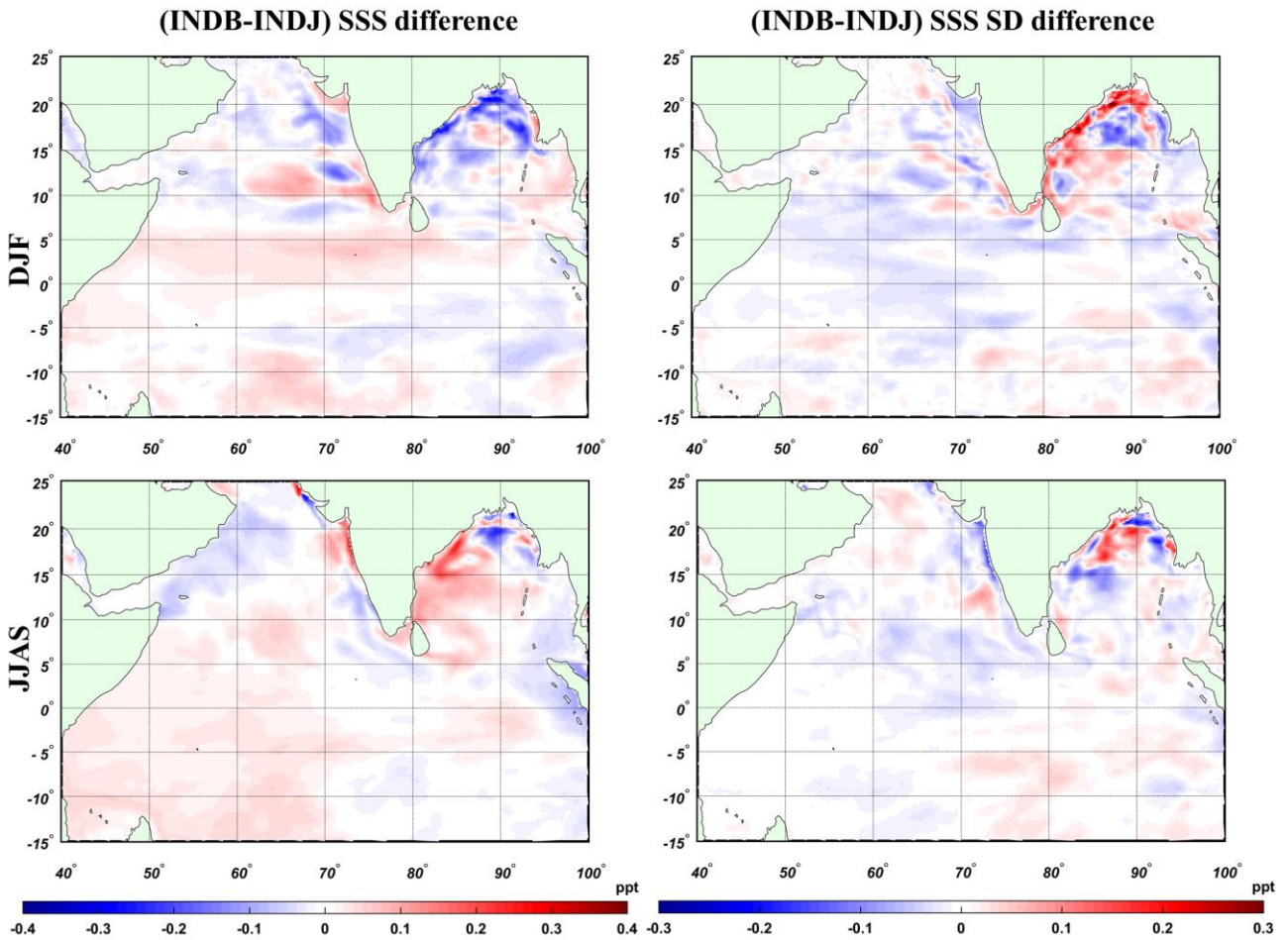


322
 323 **Figure 8.** Spatial distribution of the difference between model runs (INDB-INDJ) for SST (left column) and
 324 SST standard deviation (std., right column). SST and its std. deviation are time-averaged seasonally (DJF,
 325 JJAS) for the period 1975–2004.

326
 327 When averaging over the annual period (not shown), SST in the INDB run is also slightly
 328 lower and its deviation is higher than in INDJ. Summing up, we can say that the INDB run
 329 demonstrated the largest changes in SST occurred in summer during the active phytoplankton bloom.

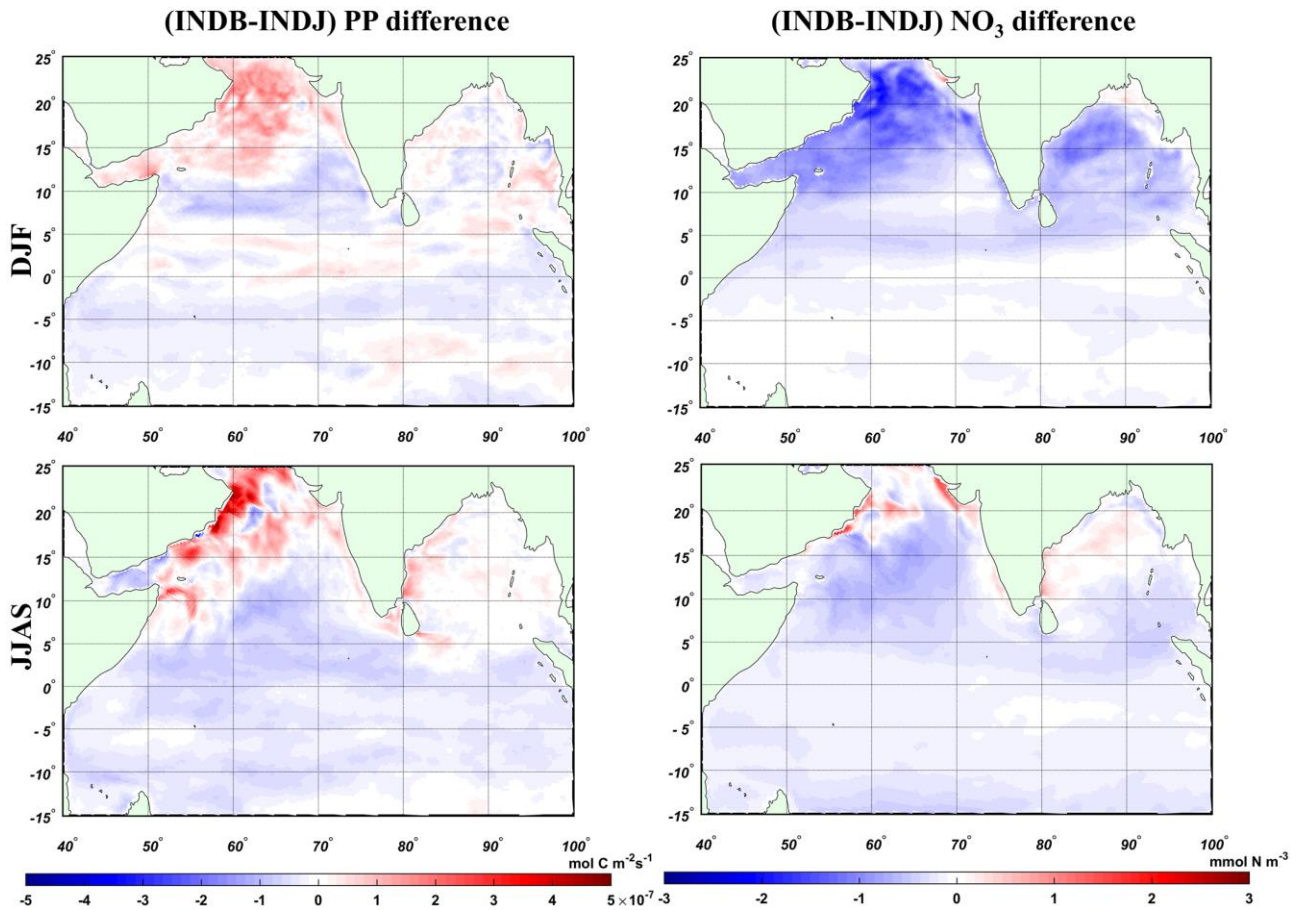
330 Figure 9 shows the spatial distribution of the SSS difference (INDB-INDJ) and the SSS
 331 standard deviation difference for the same period (1975–2004). Our results show that in all seasonal
 332 climatic averages the SSS difference between INDB and INDJ experiments is not strongly
 333 pronounced and does not generally exceed 0.2‰. The most significant changes in SSS occurs in the
 334 Bay of Bengal. Figure 9 also shows that standard deviation in the two simulations remained virtually
 335 unchanged, with the exception of the northern part of the Bay of Bengal where the INDB run showed
 336 larger seasonal deviations relative to the INDJ experiment.

337



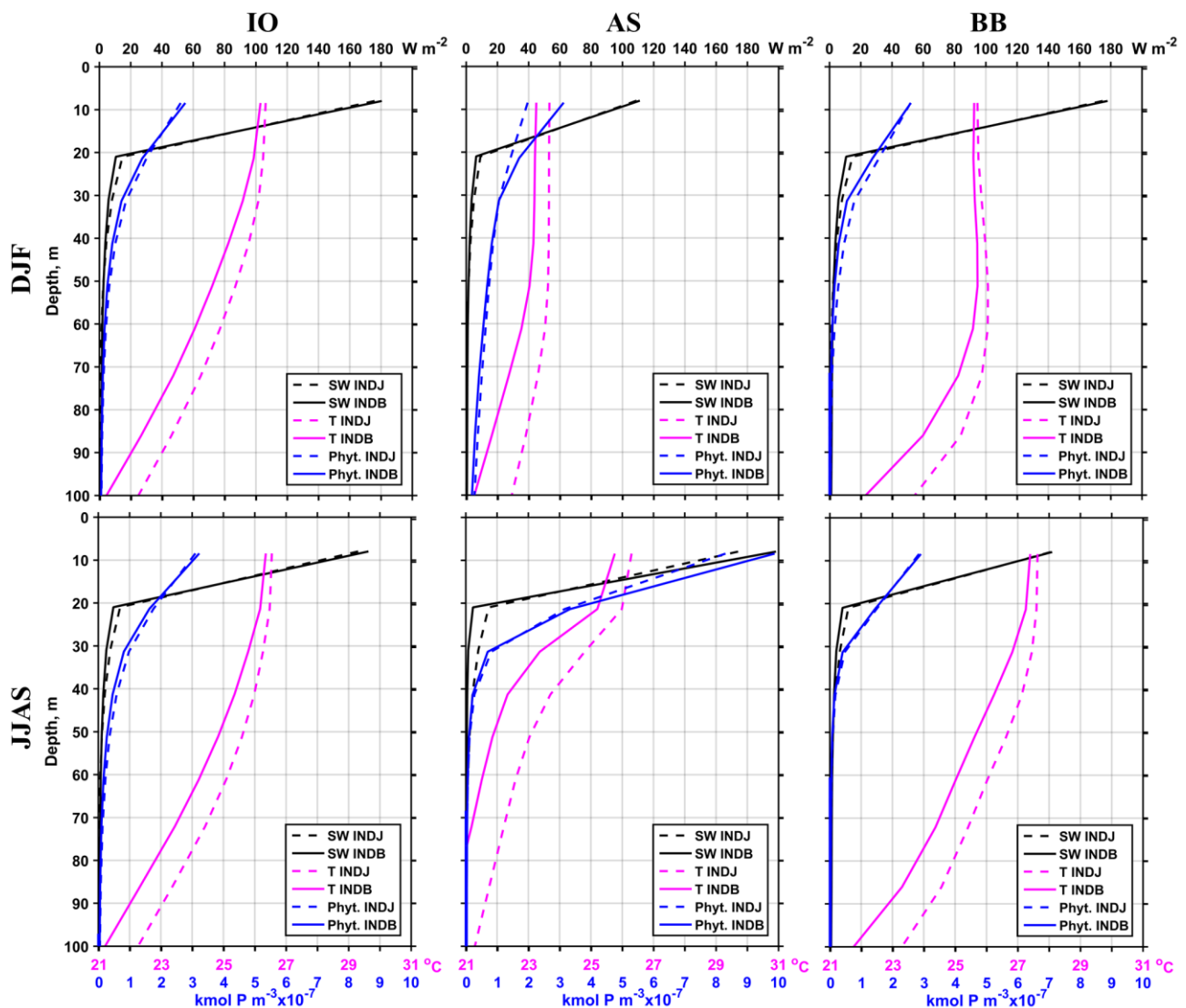
338
 339 **Figure 9.** Spatial distribution of the difference between model runs (INDB-INDJ) for SSS (left column) and
 340 SSS standard deviation (std., right column). SSS and its std. deviation are time-averaged seasonally (DJF,
 341 JJAS) for the period 1975–2004.

342
 343 *Impact of the feedback on the primary production and dissolved nitrate* is shown in Fig. 10
 344 where the differences in depth-integrated modeled phytoplankton primary production (PP) and
 345 surface concentration of dissolved nitrate (NO₃) are presented. It can be seen that the PP is higher in
 346 the INDB experiment during phytoplankton bloom periods (DJF and JJAS). The surface
 347 concentration of dissolved nitrates is lower in the INDB than in the INDJ experiment throughout the
 348 year and agrees well with the increased PP since nutrients are consumed more intensively in the
 349 surface layer.
 350



351
 352 **Figure 10.** Spatial distribution of the difference between model runs (INDB-INDJ) for PP (left column) and
 353 NO₃ (right column). PP and NO₃ are time-averaged seasonally (DJF, JJAS) for the period 1975–2004.
 354

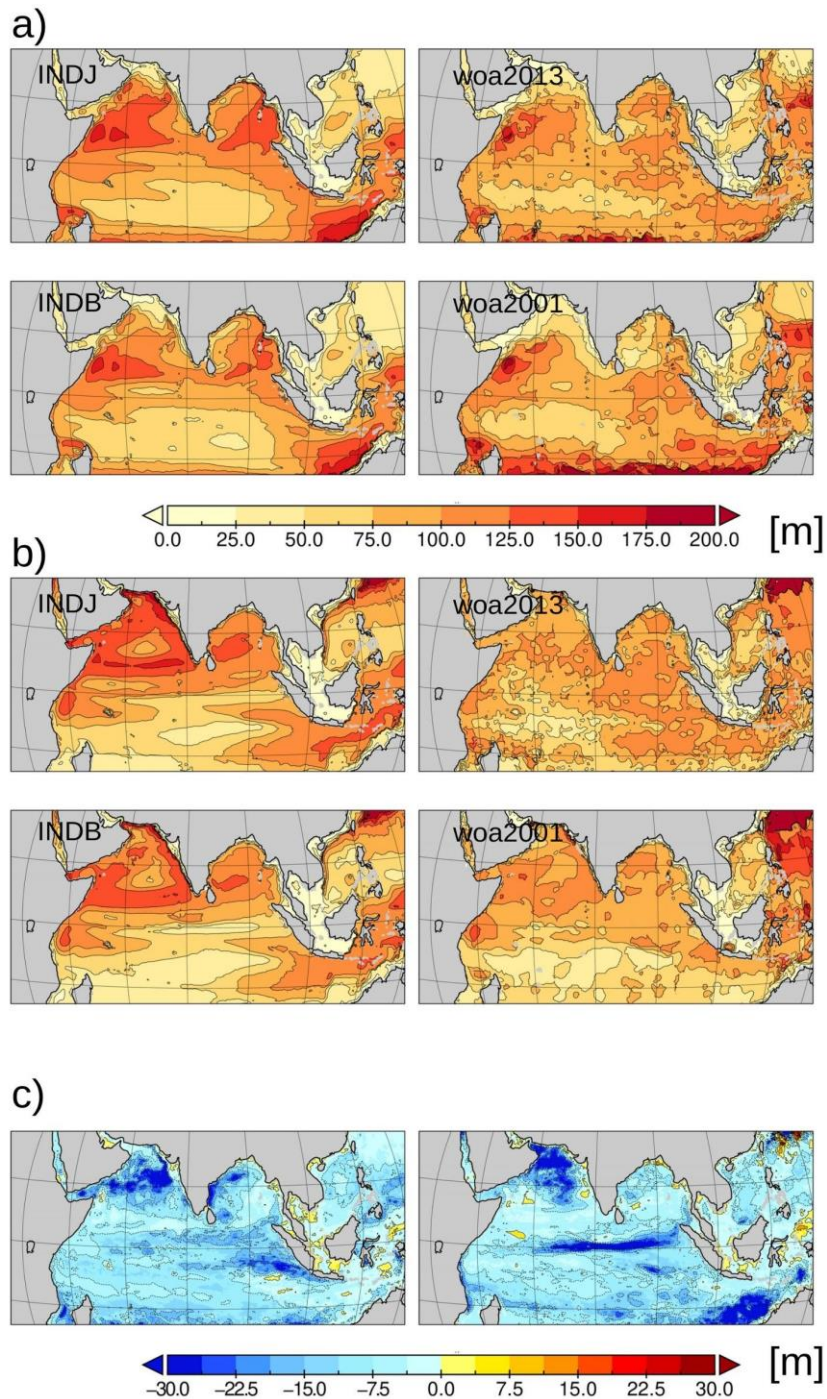
355 *Impact of the feedback on water temperature in ocean upper layers.* In order to compare the
 356 simulated water temperature in the ocean upper layers (up to 100 m depth), we chose two regions
 357 with the largest SST difference between the two model experiments (designated in Fig. 3 as AS: 60-
 358 65° E, 20-25° N and BB: 85-90°E, 15-20° N). Figure 11 shows the vertical profiles of water
 359 temperature (T), short-wave radiation (SW) and phytoplankton concentration (Phyt.) for the two
 360 model experiments considered. These vertical profiles of corresponding variables are spatially-
 361 averaged over the regions AS, BB and IO and temporally-averaged over DJF and JJAS for the period
 362 1975-2004. We note significant cooling of subsurface layers in the INDB results. For all the
 363 considered regions and the averaging periods, the amount of short-wave radiation penetrating into
 364 subsurface layers in the feedback-based experiment (INDB) is less than that in the experiment with
 365 classical light attenuation parameterization (INDJ). This is especially noticeable during the
 366 phytoplankton bloom period in the Arabian Sea in summer (JJAS).
 367



368
 369 **Figure 11.** Vertical profiles of short-wave radiation (SW), water temperature (T) and phytoplankton
 370 concentration (Phyt.) in INDJ (without ocean-atmosphere feedback through the marine ecosystem) and INDB
 371 (with the feedback) experiments.

372
 373 During summer (JJAS) the difference in short-wave radiation between the two runs reaches
 374 7-10 W/m² in the Arabian Sea at the depth of 20 m. It is reasonable to assume that this difference
 375 would be much larger at the moments of peak phytoplankton bloom when no time-averaging is made.

376 *Thermocline dynamics.* The thermocline dynamics are among the most important factors
 377 mediating the temporal and spatial shape of phytoplankton blooms and its feedback on climate. On
 378 the one hand, it acts as a barrier for the vertical exchange between nutrient-depleted surface waters
 379 and nutrient-enriched waters from deeper layers and can limit biological productivity. On the other
 380 hand, a strong thermocline can effectively reduce the local mixed layer depth and allow
 381 phytoplankton to persist longer within the euphotic layer thereby increasing the growth rate of marine
 382 algae. Moreover, the thermocline has a temperature mediating effect, with a shallower thermocline
 383 allowing the surface layer to faster adapt to atmospheric temperatures (e.g., Gröger et al., 2015). The
 384 inclusion of phytoplankton into the radiative heat transfer equation alters the vertical distribution of
 385 heat absorption and thus influences the thermocline dynamics. In the following, we test the effect of
 386 the biogeochemical feedback upon the model physics by comparing thermocline dynamics between
 387 the two runs with and without coupling (Fig. 12). Where feasible a comparison
 388



389

390

391

392

393

394

395

396

397

398

399

400

401

402

Figure 12. a) Comparison of simulated summer (JJAS) thermocline depth with thermocline depth derived from WOA data sets. b) same as (a) but for winter thermocline (DJF). c) The difference in thermocline depth between the two runs (INDB-INDJ) for JJAS (left) and DJF (right).

with WOA 2001 and WOA 2013 data is discussed. Data generally tend to be sparse in open ocean regions with less dense measuring campaigns like the Indian Ocean. Therefore, caution should be applied when interpreting thermocline dynamics derived from sparse gridded data sets like WOA. This is indicated by the irregular isolines displayed in the WOA data sets. We, therefore, do not provide a quantitative validation here but rather discuss the processes underlying the spatial pattern.

Both model simulations and WOA data show distinct gradients in thermocline depth. During the summer monsoon (Fig. 12a) the thermocline shoals to values below 25 m along the northern coast of the Arabian Sea and along the Indian coast where moisture carrying SW monsoon winds cause a positive P-E flux and maintain a vigorous runoff (Ramesh and Krishnan, 2005). Off the Somalian

403 coast and further offshore, the strong SW monsoonal winds lead to a deepening of the thermocline in
404 wide areas of the open ocean. In the model runs the extension of this area is larger than in WOA data
405 sets. In the Bay of Bengal, the model simulates a clear east-west gradient with a deeper thermocline
406 in the east compared to the west. Such a pattern is also observed to some extent, at least in the WOA
407 2001. To the south of the equator the thermocline shoals in an extended zonal band to values well
408 below 50 m. This is likewise seen in the two WOA data sets though this is less pronounced there.
409 During the winter monsoon, the very shallow thermocline in the coastal Arabian Sea strongly deepens
410 in response to changed monsoon (Fig. 12b). This seasonal change is more pronounced in the model
411 simulations but is still significant in the WOA data sets. This indicates that the seasonal variability is
412 well represented in the model near the coasts.

413 The simulated thermocline depth is almost everywhere shallower when including the
414 biogeochemical feedback (Fig. 12c) in both summer and winter. However, the spatial structure (Fig.
415 12a and 12b) is very similar, indicating that physical processes play a dominant role whereas the
416 vertical structure is controlled by biophysical processes in heat uptake. The explicit use of
417 phytoplankton in the radiated heat transfer (INDB experiment) leads to more heat absorption in the
418 upper layers and less heat absorption in lower layers. As a result, the thermocline shifts upward
419 compared to the Jerlov type absorption (INDJ experiment) which follows a simple exponential curve
420 with a constant exponent.

421

422 **3.2 Atmosphere**

423 Here we study the regional distribution of some key atmospheric fields over the South Asia
424 CORDEX region and validate them for winter (DJF) and summer (JJAS) over the 1975-2004 period.
425 In section 3.2.1 we focus on the regional distribution of 2-meter air temperature (T2M) biases relative
426 to the ERA5 reanalysis. Also, temperature differences between the INDB and INDJ experiments are
427 analysed. This allows us to gain insight into temperature changes that occur in response to the ocean
428 biogeochemical feedback. In section 3.2.2 the same procedure is followed but taking into
429 consideration the precipitation instead.

430

431 **3.2.1 Air surface temperature**

432 In both seasons the mean surface temperature in ERA5 is clearly influenced by topography
433 (Figs. 13a, 13d). The lowest values are reached on highly-elevated terrain - especially in winter. The
434 lowest temperatures are attained in world highest mountain ranges: the Himalaya, Pamir, Hindu Kush
435 and the Tibetan Plateau. The highest summer temperatures are reached along with the Indo river
436 depression and the Arabian Peninsula. In experiment INDJ the winter daily mean temperatures are
437 simulated quite well and biases are relatively small (Fig. 13b and 13e), T2M is underestimated over
438 most of the model domain, except for its northern and northwestern areas where positive biases can
439 reach up to 5 °C. The negative biases are mostly below 2 °C, except for Tibet and Himalaya, where
440 simulated T2M more than 4°C colder than ERA5 can be found. The largest errors are found in
441 depressed and/or highly-elevated regions and their values may be dependent on factors such as the
442 limited amount of meteorological stations in topographic highs and lows used for the assimilation in
443 the region and the different representation of the orography in both REMO and ERA5. JJAS T2M
444 biases are generally lower than in winter, with a similar dependence on orography. They become
445 positive over most of the Indian subcontinent with maximum values over the northern Indo river basin
446 where mean temperatures are up to 4 °C above ERA5. Over the ocean a positive bias develops in the
447 region where the monsoon winds are stronger. In general, the largest T2M biases are located in
448 regions where larger temperatures are obtained, pointing to a role of the simulated nocturnal boundary

449 layer and/or radiative fluxes. Just like for the SST, the biogeochemical feedback leads to a colder
 450 surface air temperature over most of the ocean. In DJF the cooling is stronger over the Arabian Sea
 451 and the equatorial strip, reinforcing the weak negative biases already present in INDJ. Over the land
 452 the feedback slightly improves the cold bias in northwestern and southern India but leads to a cooling
 453 in the central part. The ocean cooling induced by the feedback is also present in JJAS, with stronger
 454 values near the western coast of the Arabian Sea and the Bay of Bengal, downstream of the Monsoon
 455 winds.

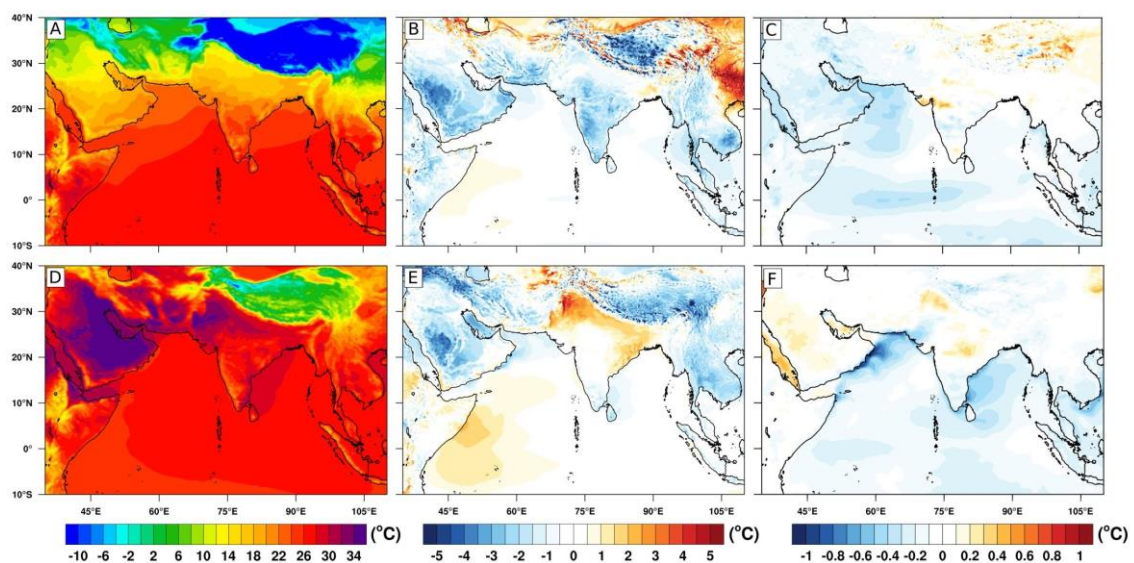
456

457 3.2.2 Monsoon precipitation

458 The monsoon season in Southern Asia is shaped by different processes which change the
 459 atmospheric circulation due to the summer strengthening of the ocean-land temperature contrast. The
 460 spatial structure of the observed monsoon precipitation is characterized by two regions of strong
 461 rainfall over land (Fig. 14a). The first is located windward, over the western coast of India, Myanmar
 462 and the southern side of the Himalayas. The second region which covers Bangladesh, central India
 463 and the eastern coast of the Indian peninsula is the area of maximum monsoon precipitation over the
 464 land. The precipitation is weaker over the northwest of India and Pakistan (Kumar et al., 2013). The
 465 complex orography and physical mechanisms involved make the simulation of the monsoon
 466 precipitation a difficult task both for global and regional models (Lucas-Picher et al., 2011).
 467 However, stand-alone simulations with REMO have shown to be able to reproduce spatial monsoon
 468 precipitation patterns rather well, although a better quantitative agreement is desirable (Kumar et al.,
 469 2014). For instance, the precipitation over south and central India is overestimated, while the
 470 precipitation over the Indo-Ganges plain is strongly underestimated. Over the ocean a wet bias is
 471 usually found over the Bay of Bengal and the southern Indian Ocean.

472 As shown in previous versions of the model (Kumar et al., 2014), ROM is able to improve the
 473 performance of REMO, simulating a more realistic precipitation. The coupling reduces the magnitude
 474 of the biases, especially in the regions where REMO has the strongest biases, near the eastern coasts
 475 of the Arabian Sea and the Bay of Bengal (Fig. 14b). It should be noted that in both INDJ and INDB
 476 experiments ROM is forced by MPI-ESM and the results are influenced by the biases of the driving
 477 ESM (e.g., Cabos et al., 2020).

478

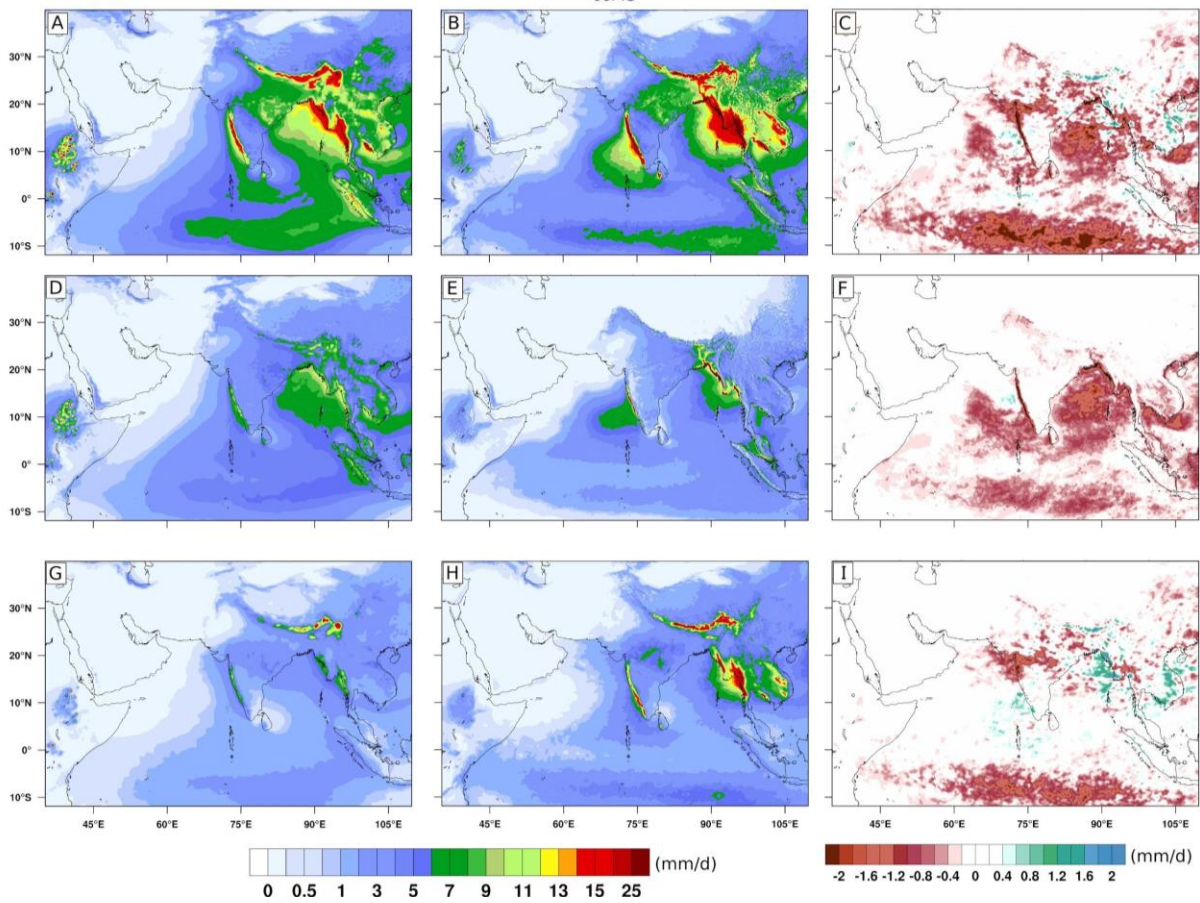


479

480 **Figure 13.** DJF (upper row) and JJAS (lower row) a) and d) 2 meter temperature ERA5 climatology b) and
 481 e) bias for the experiment INDJ; c) and f) INDB-INDJ difference.

482
483
484
485
486
487
488
489
490
491
492
493

Besides the total precipitation, in Fig. 14.d-e we show the convective (thereafter APRC) and in 14.g-h the large scale (thereafter APRL) component of the precipitation. We can see that in INDJ the main contribution to the biases over the ocean near the eastern coast of the Arabian Sea comes from APRC, while over the coastal land the main contributor is APRL. The opposite is true for the eastern coast of the Bay of Bengal, especially in Myanmar where the main contributor over the ocean and the coastal regions is APRL, with a lesser contribution from APRC. To the south of the equator, between 10° S and the equator, both components give a contribution of similar magnitude, albeit the large scale is stronger. Here, both components show a similar displacement of the region of maximum precipitation to the south, and while the magnitude of the convective precipitation is lower than in ERA5, the large scale component is stronger and more zonal than the ERA5 large scale precipitation.



494
495
496
497
498
499

Figure 14. JJAS precipitation for ERA5 (left column), INDJ experiment (middle column), and the differences between INDB and INDJ (right column) for total precipitation (upper panels); convective precipitation (middle panels), and large scale precipitation (lower panels).

500
501
502
503
504
505
506

In the INDB experiment the activation of the biogeochemical feedback leads to a drying over most of the ocean, especially over the Bay of Bengal, central and north-eastern Arabian Sea and the strip south of the equator. A clear reduction in precipitation can also be found inland, along the western Indian coast. As seen in Fig. 14.F and 14.I, the contribution of convective and large scale components to these differences varies along the regions.

We can see that APRC gives the main contribution to the total effect (in terms of precipitation) of marine biochemistry feedback over the Bay of Bengal, the central part of the Arabian Sea and the

507 coastal regions of western India. APRL gives the main contribution to the drying in the northern-
508 central India, while in the region of Myanmar it causes a wetting, thus offsetting the impact on APRC.
509 To the south of the equator, between 10° S and 0° , the impact is similar on both components of the
510 precipitation.

511

512 **4. Discussion**

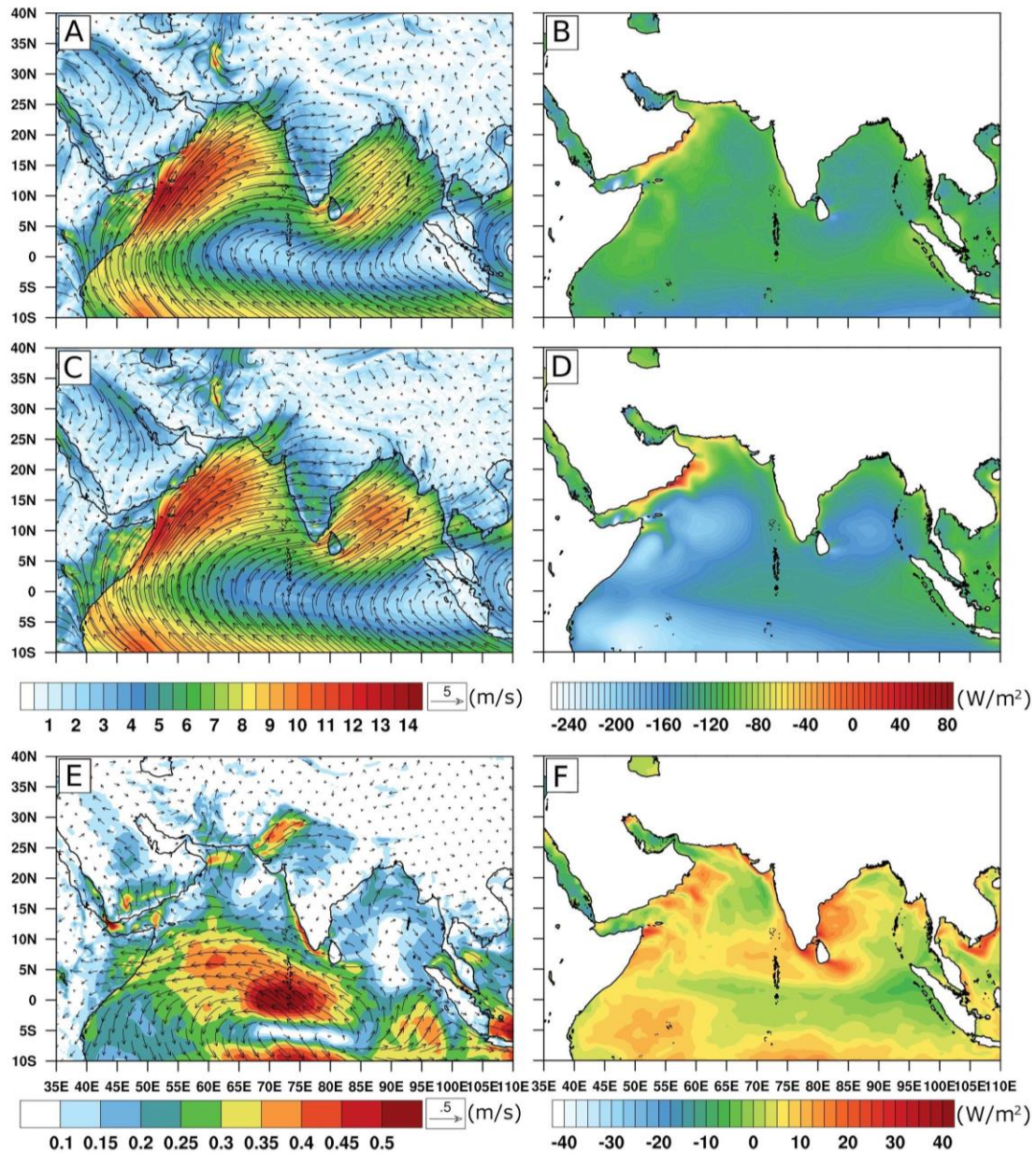
513 The effect of the feedback on the water temperature decline in the upper layers can be
514 explained as follows. In the INDB experiment, during the phytoplankton bloom period, there exists
515 more phytoplankton in the upper ocean layers than that considered according to Jerlov's climatic
516 annual-mean estimates (INDJ experiment). An increase in the amount of phytoplankton in INDB in
517 the upper layers leads to an increase of the light attenuation coefficient there, thus a smaller amount
518 of short-wave radiation penetrates into the underlying layers (this can be seen from Fig. 11). As a
519 result, the subsurface layers get colder. The thermocline shifts upward compared to the Jerlov type
520 absorption (INDJ experiment) where a simple exponential curve of light attenuation is implemented.
521 Despite the shallower thermocline in INDB, this run shows overall cooler SSTs than INDJ (Fig. 8).
522 This is somewhat counter-intuitive as a lower mixed-layer depth should reduce the mixing with cooler
523 waters from depth leading to overall higher SSTs in run INDB. However, the different solutions of
524 the radiative equation used in INDB and INDJ will also affect the total absorbed radiation which
525 makes it difficult to link the direct effect of changed thermocline depth to the difference in SSTs.
526 Given the widespread cooling of SSTs in INDB (Fig. 8) however, it is likely that the parameterization
527 of absorption in INDB leads to a general decrease in total absorption compared to the Jerlov solution.
528 Also, it may be assumed that during the vertical mixing process the cold water may enter the upper
529 ocean layers, thus the upper-mixed layer temperature declines, and so does SST, although for SST
530 this effect is less pronounced because it can be more influenced by other ocean-atmosphere heat
531 fluxes. Thus, during the period of active heating of the upper ocean layers the heat in the INDB
532 experiment is redistributed differently than in the INDJ and, as a result, a significant cooling of the
533 subsurface layers occurs. At the same time, the spatial pattern of SST cooling is not homogeneous
534 (see Fig. 8) that can be explained by other heat fluxes, which, in contrast to short-wave radiation, are
535 absorbed by the upper 1-meter layer of the ocean almost completely. In future studies we are planning
536 to analyze this mechanism in detail and to evaluate the impact of advection.

537 Thus, the main impact of including the biogeochemical coupling in the Indian Ocean is a
538 shallower thermocline with cascading effects on model physics like altered SST which further
539 translates into altered atmosphere dynamics. Likewise, due to the temporarily varying chlorophyll-a
540 concentrations in the surface layer and subsequent variable heat absorption, SSTs are by far more
541 variable in run INDB than in run INDJ.

542 The higher phytoplankton primary production in INDB (Fig. 10) is most likely the effect of
543 the lowered mixed-layer depth which allows phytoplankton to prevail longer in the euphotic layer.
544 This effect is more pronounced to the north of 10° N where the thermocline is relatively deep (and a
545 reduction of the mixed-layer depth is most effective). In regions where the thermocline is generally
546 shallower (to the south of 10° N) this effect is of minor importance as light is less limiting there.

547 During JJAS, the simulated wind in INDJ is slightly weaker than in ERA5 in the Arabian Sea
548 but stronger in the Bay of Bengal (compare Fig. 15.a and 15.c).

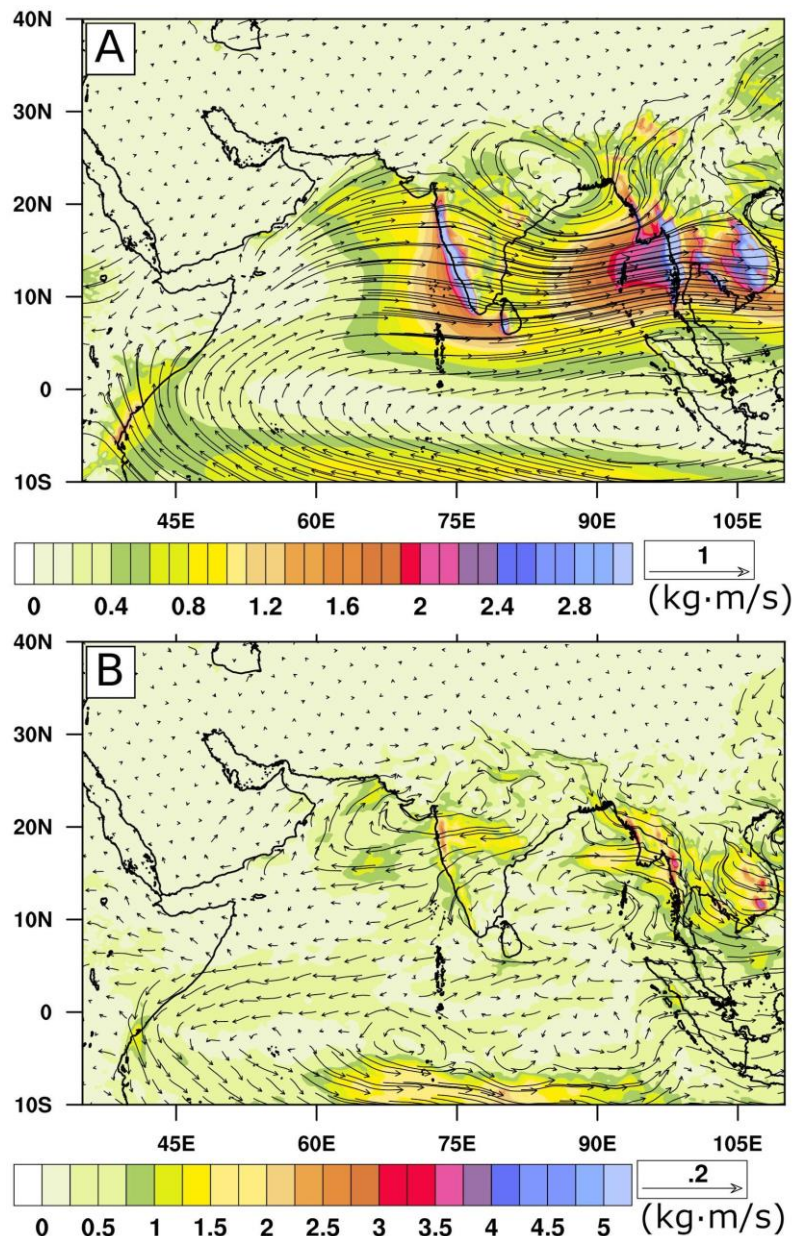
549



550
 551 **Figure 15.** JJAS wind (left column) and latent heat (right column) for ERA5 (upper panels); INDJ experiment
 552 (middle panels), and (INDB-INDJ) difference (lower panels).
 553

554 In the latter, stronger winds lead to stronger latent heat fluxes, while the opposite is true for
 555 the Arabian Sea where the weaker wind is associated with a stronger latent heat (Fig 15.b and Fig
 556 15.d). This points to a different nature of the relationship between wind speed and latent heat in both
 557 regions that, nevertheless, lead to stronger heat flux in both regions. The monsoon winds bring drier
 558 air into the Arabian Sea because it flows over colder water all the way from the equatorial region.
 559 Although the cold bias here leads also to a decrease of surface humidity, as the SST bias is lower, the
 560 surface humidity bias is lower. The resulting increase of the sea-air humidity difference overcomes
 561 the decrease of the wind, thus giving a stronger latent heat flux. This is not true for the western coast
 562 where most of the air comes from land (Wu et al., 2007). In the Bay of Bengal the increase in latent
 563 heat is mainly associated with the simulated winds which are stronger than in ERA5. In the INDB
 564 experiment the biogeochemical feedback causes a further cooling over the basin (Fig. 8) and this
 565 cooling causes a further drying over most of the domain, especially over the land in regions that are
 566 downstream of the monsoon winds. The drying is related to changes both in convection activity and

567 moisture transport. Figure 16.a shows the horizontal transport of cloud water for the INDJ experiment.
 568 This figure shows the contribution of the large-scale circulation to the monsoon rain. The Arabian
 569 Sea winds are charged with moisture in their path to the Indian subcontinent and Sri Lanka,
 570 contributing to the large scale precipitation in the eastern part of the basin and the coastal regions
 571 (Fig. 14.h). The wind, which loses moisture over the land, is again recharged in his way over the Bay
 572 of Bengal, contributing to the strong precipitation in the eastern part of the Bay of Bengal, Myanmar
 573 and southeastern Asia. It is noteworthy the recirculation of cloud water in northeastern India due to
 574 the presence of the Himalayan range which influences the amount of precipitation there. The marine
 575 biochemistry feedback affects the precipitation over the Arabian Sea and the Bay of Bengal in
 576 different ways. From one side, it reduces the transport of humidity across the equator towards the
 577 eastern part of the basin, reducing the large scale precipitation there and in the adjacent coastal
 578 regions, reinforcing the effect of the colder water on the convective precipitation. In the Bay of Bengal
 579 the feedback reinforces the transport of humidity, increasing the large scale precipitation, contouring
 580 the decrease of convective precipitation due to the SST cooling (Fig 16.b).
 581



582 **Figure 16.** JJAS horizontal transport of cloud water in INDJ (a) and INDB-INDJ difference (b)
 583

584

585 **5. Conclusions**

586 A regional Earth System Model based on the ROM model (Sein et al., 2015) has been
587 implemented for the CORDEX South Asia region. We use the model to investigate the effect of one
588 of the marine biogeochemical feedbacks, which affects the attenuation of the short-wave radiation in
589 the water, upon the regional climate. To this end we carry out two model runs for the period 1920–
590 2005 with CMIP5 historical forcing. The runs differ in various parameterizations of the attenuation
591 of short-wave radiation into the ocean.

592 Our simulations capture the main fundamental features of the intra-annual dynamics of the
593 marine ecosystem in this region. This is a good result for a global biogeochemical model that works
594 with only one type of phytoplankton. Some overestimation of the chlorophyll-a surface concentration
595 compared to satellite data is acceptable due to the known uncertainties in the estimates of the C:Chla
596 ratio which is set constant in the model.

597 In the experiment where the feedback is activated the average SST is lower over most of the
598 domain than in the simulation without the feedback. The greatest deviations (more than 1 °C) in SST
599 between the two runs occur in the summer period during the phytoplankton bloom. During the period
600 of active heating of the upper layers (spring and summer) the short-wave radiation calculated by the
601 simulation with the feedback activated is more strongly absorbed in the upper ocean layers, a
602 significant cooling of subsurface layers occurs (up to 1-1.5 °C) and the thermocline shifts upward
603 compared to the Jerlov type absorption. In other words, the explicit taking into account the
604 phytoplankton concentration while calculating the short-wave radiation attenuation leads to a cooling
605 of the subsurface layers. At the same time, the spatial pattern of SST cooling is not homogeneous that
606 can be explained by other heat fluxes, which, in contrast to short-wave radiation, are absorbed by the
607 upper 1-meter layer of the ocean almost completely. The phytoplankton primary production and its
608 deviation in the feedback-based simulation turned out to be higher, especially during periods of winter
609 and summer phytoplankton blooms. The feedback-based simulation also showed the lower surface
610 concentration of dissolved nitrates almost the whole year since the primary production was higher
611 and more nutrients were consumed by phytoplankton.

612 Both simulations reproduce adequately the precipitation climatology for all seasons. In
613 particular, the spatial pattern of the monsoon precipitation is well simulated, albeit with some
614 systematic wet biases which are stronger over the eastern parts of the Arabian Sea and the Bay of
615 Bengal and the adjacent coastal regions. We found that the marine biogeochemistry feedback also
616 affects the amount of precipitation in the model, leading to a drying over most of the basin in the
617 monsoon season. The associated SST cooling leads in general to a reduction of the precipitation but
618 affects in different ways the two components of the precipitation. In the Arabian Sea the reduction of
619 the transport of humidity across the equator leads to a reduction of the large scale precipitation in the
620 eastern part of the basin, reinforcing reduction of the convective precipitation. In the Bay of Bengal
621 the feedback increases the large scale precipitation, contouring the decrease of convective
622 precipitation due to the SST cooling.

623 Thus, the main impacts of including the biogeochemical coupling in the Indian Ocean include
624 the enhanced phytoplankton primary production, a shallower thermocline and decreased SST, with
625 cascading effects upon the model ocean physics which further translates into altered atmosphere
626 dynamics.

627

628 **Acknowledgements.** This research was performed in the framework of the state assignment of the
629 Ministry of Science and Higher Education of Russia (theme No. 0149-2019-0015). The work was

630 supported by the Russian Science Foundation (Project 19-47-02015 "Impact of climate change on
631 South Asia extremes: A high-resolution regional Earth System Model assessment"). Pankaj Kumar
632 was supported by the Department of Science and Technology (DST), Govt. of India, grant number
633 DST/INT/RUS/RSF/P-33/G. Simulations were performed on the German Climate Computing
634 Center (DKRZ). The model data used in the paper are available at
635 https://swiftbrowser.dkrz.de/tcl_s/SSG22k1U4mIXVr
636

637 **References**

- 638 Arakawa, A., and V. R. Lamb (1977), Computational design of the basic dynamical processes
639 of the UCLA general circulation model, *Methods Comput. Phys.*, 17, 173–265.
- 640 Bolch, T., Kulkarni, a., Kaab, a., Huggel, C., Paul, F., Cogley, J. G., et al. (2012). The State
641 and Fate of Himalayan Glaciers. *Science*, 336(6079), 310–314.
642 <https://doi.org/10.1126/science.1215828>
- 643 Choudhury, A. K., & Pal, R. (2010). Phytoplankton and nutrient dynamics of shallow coastal
644 stations at Bay of Bengal, Eastern Indian coast. *Aquatic Ecology*, 44(1), 55-71.
- 645 Cogley J. G., Present and future states of Himalaya and Karakoram glaciers. *Ann. Glaciol.* 52,
646 69(2011).
- 647 D'Asaro, E., Altabet, M., Kumar, N. S., Ravichandran, M. (2019) Structure of the Bay of
648 Bengal oxygen deficient zone. *Deep Sea Research Part II: Topical Studies in Oceanography*,
649 <https://doi.org/10.1016/j.dsr2.2019.104650>
- 650 De U.S., R.K.Dube and G.S.Prakasa Rao, Extreme Weather Events over India in the last 100
651 years, *J. Ind. Geophys. Union* (July 2005) Vol.9, No.3, pp.173-187
- 652 De, T. K., De, M., Das, S., Chowdhury, C., Ray, R., & Jana, T. K. (2011). Phytoplankton
653 abundance in relation to cultural eutrophication at the land-ocean boundary of Sunderbans, NE Coast
654 of Bay of Bengal, India. *Journal of Environmental Studies and Sciences*, 1(3), 169.
- 655 Dube, S. K., Rao, A. D., Sinha, P. C., Murty, T. S., & Bahulayan, N. (1997). Storm surge in
656 the Bay of Bengal and Arabian Sea The problem and its prediction. *Mausam*, 48(2), 283-304.
- 657 Giorgi, F., (2006), Regional climate modeling: status and perspectives. *J Phys IV France.*, 139, 101–
658 18. <http://dx.doi.org/10.1051/jp4:2006139008>.
- 659 Eric D'Asaro, Mark Altabet, N. Suresh Kumar, M. Ravichandran, Structure of the Bay of
660 Bengal oxygen deficient zone, *Deep Sea Research Part II: Topical Studies in Oceanography*, 2019,
661 104650, ISSN 0967-0645, <https://doi.org/10.1016/j.dsr2.2019.104650>
- 662 Goswami B. N., V. Venugopal, D. Sengupta, M. S. Madhusoodanan, Prince K. Xavier (2006),
663 Increasing Trend of Extreme Rain Events Over India in a Warming Environment, *Science* 01 Dec
664 2006: Vol. 314, Issue 5804, pp. 1442-1445. DOI:10.1126/science.1132027
- 665 Gröger, M., Maier-Reimer, E., Mikolajewicz, U., Moll, A., and Sein, D.: NW European shelf
666 under climate warming: implications for open ocean – shelf exchange, primary production, and
667 carbon absorption, *Biogeosciences*, 10, 3767–3792, <https://doi.org/10.5194/bg-10-3767-2013>, 2013.
- 668 Gröger, M., Dieterich, C., Meier, Markus HEM, Schimanke, S. (2015), Thermal air-sea
669 coupling in hindcast simulations for the North Sea and Baltic Sea on the NW European shelf, *Tellus*
670 *A*, 67, 26911, doi: 10.3402/tellusa.v67.26911.
- 671 Hagemann, S., and L. Dumenil (1998), A parameterization of the lateral waterflow for the
672 global scale, *Clim. Dyn.*, 14, 17–31.
- 673 Hagemann, S., and L. Dumenil Gates (2001), Validation of the hydrological cycle of ECMWF
674 and NCEP reanalyses using the MPI hydrological discharge model, *J. Geophys. Res.*, 106, 1503–
675 1510.
- 676 Ilyina, T., K. D. Six, J. Segsneider, E. Maier-Reimer, H. Li, and I. N_u~nez-Riboni (2013),
677 Global ocean biogeochemistry model HAMOCC: Model architecture and performance as component
678 of the MPI-Earth system model in different CMIP5 experimental realizations, *J. Adv. Model. Earth*
679 *Syst.*, 5, doi:10.1029/2012MS000178.
- 680 IPCC, 2014: Climate Change 2014: Synthesis Report. Contribution of Working Groups I, II
681 and III to the Fifth Assessment Report of the Intergovernmental Panel on Climate Change [Core
682 Writing Team, R.K. Pachauri and L.A. Meyer (eds.)]. IPCC, Geneva, Switzerland, 151 pp.

683 Jacob, D. (2001), A note to the simulation of the annual and interannual variability of the
684 water budget over the Baltic Sea drainage basin, *Meteorol. Atmos. Phys.*, 77(1-4), 61–73.

685 Jacob, D., et al. (2001), A comprehensive model intercomparison study investigating the water budget
686 during the BALTEX-PIDCAP period, *Meteorol. Atmos. Phys.*, 77(1-4), 19–43.

687 Jerlov, N. G. *Marine Optics*. Elsevier, Amsterdam. (1976)

688 Jungclaus, J. H., N. Fischer, H. Haak, K. Lohmann, J. Marotzke, D. Matei, U. Mikolajewicz,
689 D. Notz, and J. S. von Storch (2013), Characteristics of the ocean simulations in MPIOM, the ocean
690 component of the MPI-Earth system model, *J. Adv. Model. Earth Syst.*, 5, 422–446,
691 doi:10.1002/jame.20023.

692 Kumar, P., Wiltshire, A., Mathison, C., Asharaf, S., Ahrens, B., Lucas-Picher, P., et al. (2013).
693 Downscaled climate change projections with uncertainty assessment over India using a high
694 resolution multi-model approach. *Science of the Total Environment*, 468–469, S18–S30.
695 <https://doi.org/10.1016/j.scitotenv.2013.01.051>

696 Kumar, P. , Sein, D. , Cabos, W. and Jacob, D. (2014) Improvement of simulated monsoon
697 precipitation over South-Asia with a regionally coupled model ROM / Barring, L. , Reckermann,
698 M. , Rockel, B. and Rummukainen, M. (editors) , In: 3rd International Lund Regional-Scale Climate
699 Modelling Workshop 21st Century Challenges in Regional Climate Modelling: Workshop
700 proceedings, Lund, Sweden, 16-19 June 2014, (International Baltic Earth Secretariat Publications ;
701 3), Geesthacht, International Baltic Earth Secretariat, 434 p. .

702 Lucas-Picher, P., J.H. Christensen, F. Saeed, P. Kumar, S. Asharaf, B. Ahrens, et al. (2011),
703 Can regional climate models represent the Indian monsoon? *J Hydrometeor.*, 12, 849–68.
704 <http://dx.doi.org/10.1175/2011JHM1327.1>.

705 Maier-Reimer, E. (1993), Geochemical cycles in an ocean general circulation model:
706 Preindustrial tracer distributions, *Global Biogeochem. Cycles*, 7, 645–677.

707 Maier-Reimer, E., I. Kriest, J. Segschneider, and P. Wetzol (2005), Technical description of
708 the HAMburg Ocean Carbon Cycle model, version 5.1 (HAMOCC5.1), and of its interface to
709 MPIOM. Reports on Earth System Science, Max Planck Institute for Meteorol., Hamburg. [Available
710 at <http://edoc.mpg.de/get.epl?fid517575&did5249293&ver50>.]

711 Majewski, D. (1991), The Europa modell of the Deutscher Wetterdienst, in Seminar
712 Proceedings ECMWF, vol. 2, pp. 147–191, ECMWF, Reading, U. K.

713 Marsland, S. J., H. Haak, J. H. Jungclaus, M. Latif, and F. Roeske (2002), The Max-Planck-
714 Institute global ocean/sea ice model with orthogonal curvilinear coordinates, *Ocean Modell.*, 5(2),
715 91–126.

716 Mukhopadhyay, S. K., Biswas, H. D. T. K., De, T. K., & Jana, T. K. (2006). Fluxes of nutrients
717 from the tropical River Hooghly at the land–ocean boundary of Sundarbans, NE Coast of Bay of
718 Bengal, India. *Journal of Marine Systems*, 62(1-2), 9-21.

719 Omid Mazdiyasni, Amir Agha, Kouchak, Steven J. Davis, Shahrbanou Madadgar, Ali
720 Mehran, Elisa Ragno, Mojtaba Sadegh, Ashmita Sengupta, Subimal Ghosh, C. T. Dhanya and
721 Mohsen Niknejad Increasing probability of mortality during Indian heat waves *Science Advances* 07
722 Jun 2017: Vol. 3, no. 6, e1700066 DOI: 10.1126/sciadv.1700066

723 Pai, D.S., Thapliyal, V. & Kokate, P.D., 2004. Decadal variation in the heat and cold waves
724 over India during 1971-2000, *Mausam*, 55, 2 (April 2004), 281-292.

725 Ramesh, K. V., and Krishnan, R. (2005), Coupling of mixed layer processes and thermocline
726 variations in the Arabian Sea, *J. Geophys. Res.*, 110, C05005, doi:10.1029/2004JC002515.

727 Roeckner, E., et al. (2003), The atmospheric general circulation model ECHAM 5. PART I:
728 Model description, Rep. 349, MPI Jour. Meteorol., Hamburg, Germany.

729 Roeckner, E., K. Arpe, L. Bengtsson, M. Christoph, M. Claussen, L. Dumenil, M. Esch, M.
730 Giorgetta, U. Schlese, and U. Schulzweida (1996), The Atmospheric General Circulation Model
731 ECHAM-4: Model description and simulation of present-day climate, Rep. 218, MPI Jour. Meteorol.,
732 Hamburg, Germany.

733 Ryabchenko, V. A., Gorchakov, V. A., & Fasham, M. J. R. (1998). Seasonal dynamics and
734 biological productivity in the Arabian Sea Euphotic Zone as simulated by a three-dimensional
735 ecosystem model. *Global Biogeochemical Cycles*, 12(3), 501-530.

736 Sattar, M. A., Kroeze, C., & Stokal, M. (2014). The increasing impact of food production on
737 nutrient export by rivers to the Bay of Bengal 1970–2050. *Marine pollution bulletin*, 80(1-2), 168-
738 178.

739 Schwendike, J., P. Govekar, M. J. Reeder, R. Wardle, G. J. Berry, and C. Jakob (2014),
740 Local Partitioning of the overturning circulation in the tropics and the connection to the Hadley and
741 Walker circulations, *J. Geophys. Res. Atmos.*, 119, 1322–1339, doi:10.1002/2013JD020742.

742 Sein, D. V., U. Mikolajewicz, M. Gröger, I. Fast, W. Cabos, J. G. Pinto, S. Hagemann, T.
743 Semmler, A. Izquierdo, and D. Jacob (2015), Regionally coupled atmosphere-ocean-sea ice-marine
744 biogeochemistry model ROM:1. Description and validation, *J. Adv. Model. Earth Syst.*, 7, 268–304,
745 doi:10.1002/2014MS000357.

746 Seitzinger, S. P., Harrison, J. A., Dumont, E., Beusen, A. H., & Bouwman, A. F. (2005).
747 Sources and delivery of carbon, nitrogen, and phosphorus to the coastal zone: An overview of Global
748 Nutrient Export from Watersheds (NEWS) models and their application. *Global Biogeochemical*
749 *Cycles*, 19(4). doi:10.1029/2005GB002606.

750 Seitzinger, S. P., Kroeze, C., Bouwman, A. F., Caraco, N., Dentener, F., & Styles, R. V.
751 (2002). Global patterns of dissolved inorganic and particulate nitrogen inputs to coastal systems:
752 Recent conditions and future projections. *Estuaries*, 25(4), 640-655.

753 de Sherbinin, A. Climate change hotspots mapping: what have we learned?. *Climatic*
754 *Change* 123, 23–37 (2014) doi:10.1007/s10584-013-0900-7

755 Szabo S., Robert J. Nicholls, Barbara Neumann, Fabrice G. Renaud, Zoe Matthews, Zita
756 Sebesvari, Amir AghaKouchak, Roger Bales, Corrine Warren Ruktanonchai, Julia Kloos, Efi
757 Foufoula-Georgiou, Philippus Wester, Mark New, Jakob Rhyner & Craig Hutton (2016) Making
758 SDGs Work for Climate Change Hotspots, *Environment: Science and Policy for Sustainable*
759 *Development*, 58:6, 24-33, DOI: 10.1080/00139157.2016.1209016

760 Tasnim, K. M., Shibayama, T., Esteban, M., Takagi, H., Ohira, K., & Nakamura, R. (2015).
761 Field observation and numerical simulation of past and future storm surges in the Bay of Bengal: case
762 study of cyclone Nargis. *Natural Hazards*, 75(2), 1619-1647.

763 Taylor, K. E., R.J. Stouffer, and G.A. Meehl (2012), An overview of CMIP5 and the
764 experiment design, *Bull. Am. Meteorol. Soc.*, 93, 485–498.

765 Turco, M., E. Palazzi, J. von Hardenberg, A. Provenzale, Observed climate change hotspots.
766 *Geophys. Res. Lett.* 42, 3521–3528 (2015).

767 Winkelmann, R., Martin, M. A., Haseloff, M., Albrecht, T., Bueler, E., Khroulev, C., and
768 Levermann, A.: The Potsdam Parallel Ice Sheet Model (PISM-PIK) – Part 1: Model description, *The*
769 *Cryosphere*, 5, 715–726, <https://doi.org/10.5194/tc-5-715-2011>, 2011.

770 WMO, 2001. WMO statement on the states of the global climate in 2000, WMO No. 920.

771 WMO, 2008. WMO statement on the states of the global climate in 2008, WMO No. 1039.

772 Wu, R., Kirtman, B. P., and Pegion, K. (2007), Surface latent heat flux and its relationship
773 with sea surface temperature in the National Centers for Environmental Prediction Climate Forecast

774 System simulations and retrospective forecasts, *Geophys. Res. Lett.*, 34, L17712,
775 doi:10.1029/2007GL03075